Botero, Yesica L.; Canales-Mahuzier, Andrés; Serna-Guerrero, Rodrigo; López-Valdivieso, Alejandro; Benzaazoua, Mostafa; Cisternas, Luis A.

Physical-chemical study of IPETC and PAX collector's adsorption on covellite surface

Published in:
Applied Surface Science

DOI:
10.1016/j.apsusc.2022.154232

Published: 15/11/2022

Document Version
Peer-reviewed accepted author manuscript, also known as Final accepted manuscript or Post-print

Physical-chemical study of IPETC and PAX collector's adsorption on covellite surface

Yesica. L. Botero[a,d*], Andrés Canales-Mahuzier[a], Rodrigo Serna-Guerrero[b], Alejandro López-Valdivieso[c], Mostafa Benzaazoua[d] and Luis A. Cisternas[a]

[a] Departamento de Ingeniería Química y Procesos de Minerales, Universidad de Antofagasta, Antofagasta, Chile

[b] Department of Chemical and Metallurgical Engineering, School of Chemical Engineering, Aalto University, PO Box 16200, FI-00076 Aalto, Finland

[c] Instituto de Metalurgia, Universidad Autónoma de San Luis de Potosi, San Luis Potosi, Mexico

[d] Institut de Recherche en Mines et Environnement (IRME), Université du Québec en Abitibi-Témiscamingue, 445 Boul. Université, Rouyn-Noranda, QC J9X 5E4, Canada

[*]Corresponding author: yesica.botero@uantof.cl

Highlights

- Collectors IPETC and PAX have a marked effect on the covellite flotation.
- XPS shows that the covellite surface has two oxidation states, Cu(I) and Cu(II).
- IPETC adsorption on covellite is realized through S of the collector with Cu atoms.
- PAX adsorption on CuS is realized through =S and –S of the collector with Cu atoms.

Abstract

The adsorption mechanisms of the collectors O-isopropyl-N-ethyl thionocarbamate (IPETC) and potassium amyl xanthate (PAX) on a covellite surface were studied through microflotation tests, Fourier-transform infrared spectroscopy (FT-IR), X-ray photoelectron spectroscopy (XPS), and density functional theory (DFT) calculations. The microflotation test demonstrated that the collectors have a marked effect on the covellite flotation and that covellite flotation is not pH-dependent. The FT-IR spectra for covellite treated with IPETC and PAX collectors at pH 8 and 11 does not differ significantly. For IPETC, the leading adsorption –C(=S) –NH group vibration was identified, and the NH stretching band is absent from both spectra. The spectra show the frequencies for the PAX, Cu-amylxanthate (CuAX), and $(AX)_2$ dixantogen that formed. The XPS spectra showed that the adsorption mechanism of PAX on the covellite surface is principally through C 1s and S 2p. The adsorption mechanism of IPETC on the covellite surface suggests that the bond is enabled through the =S element of the collector with Cu atoms in the covellite surface. Finally, the DFT calculations predict that for IPETC the bond with copper only occurred through the C=S group. For PAX, the bond with copper occurred through the C=S and C–S groups.

Key words: covellite; collector adsorption; thionocarbamate; amyl xanthate; density functional theory.

1. Introduction

Copper is mainly derived from primary sources. This is a significant issue in the mining sector because the global reserves of copper are expected to decrease dramatically by 2050, with a corresponding ore grade decline to approximately 0.1 %. Thus, as the copper demand increases, the ore grade decreases [1]. The high demand for copper is associated with the growth in global population and economic development, increasing the consumption of this metal in several economic sectors, notably wiring, plumbing, and electricity [2]. This has been further exasperated by the global targets to reduce greenhouse gas emissions, which include a transition towards electric vehicles that use four times as much copper as petroleum-fueled cars [3]. This shift also requires investments in infrastructure to provide sufficient charging stations[3].

For this reason, increasing copper extraction efficiency is mandatory. Currently, chalcopyrite is the leading mineral from which copper is extracted. Nevertheless, a possible way to enhance copper supply is to exploit other minerals, such as covellite. Covellite can be found in ore, waste rock, and tailing deposits. For instance, Burrows et al. [4] reported a copper–gold deposit in Eastern Sumbawa, Indonesia, where copper occurs exclusively as covellite associated with pyrite (with 0.6% Cu). Lam et al. [5] reported a copper tailings site with 0.21 % chalcopyrite, 0.09 % chalcocite, and 0.10 % covellite. Thus, historical tailings sites can be used as a source of copper extraction if mineral species other than chalcopyrite are targeted. According to its chemical formula, it is worth mentioning that covellite has almost double the amount of copper that chalcopyrite. In this sense, even if the ore has a low level of covellite compared to chalcopyrite, it could provide a significant amount of copper. For instance, Tian et al. [6] reported on a mineral concentrate, wherein the copper-bearing minerals were mainly chalcocite (11 %), chalcopyrite (8 %), bornite (4.3 %), and covellite (1 %). The chalcocite, chalcopyrite, and bornite contributed 45.11 %, 29.6 %, and 15.72 % of the copper, respectively. Although the covellite only comprised 1%, it contributed 8.6% of the total copper in the concentrate. The relative level of covellite in the concentration allows us to identify the importance of this mineral as a copper supplier.

Interest in covellite has increased because it is utilized in optics—thanks to its excellent semiconductor properties—and as a cathode material, but this latter is usually synthetic covellite [7,8]. In spite of this, only a few studies have been dedicated to covellite flotation [8–11]. These works have taken different focuses: the electrochemical behavior of covellite when interacting with collectors, adsorption behavior when using adsorption density measurements, the effect of calcium hypochlorite ($Ca(ClO)_2$) as a depressor on the flotation separation of covellite–pyrite, and a theoretical study of the interaction of surfactants on the covellite surface. Thus, there is a dearth of information about covellite flotation and the interaction mechanism between covellite and reagents (particularly collectors and pH modifiers). Consequently, the present work is focused on an adsorption study of collectors O-isopropyl-N-ethyl thionocarbamate (IPETC) and potassium amyl xanthate (PAX) at different pH levels on a covellite surface, using FT-IR, XPS characterization techniques, and computational modeling via the DFT method.

To understand the chemical interactions between covellite and collectors, we must discern the chemical properties and structure of covellite and the collectors under study. Several works have studied covellite's topological and electrochemical properties using modeling methods [12–15]. Covellite has a complex structure with hexagonal symmetry, described as tetrahedral (CuS_4) and trigonal (CuS_3) (see Fig. 1) [16]. The arrangements of atoms are generally analyzed along the (001) direction, where the trigonal planar arrangement is attributed to Cu(1)-S(1) bonding, and tetrahedral arrangement is attributed to Cu(2)-S(2) bondings, which relate to the following the sequence:

(Cu(2)-S(2)$_4$)-(Cu(1)-S(1)$_3$)-(Cu(2)-S(2)$_4$). The Cu(1), Cu(2), S(1), and S(2) correspond to Cu(I), Cu(II), S^{2-} and S_2^{2-}, respectively. The disulfide bond (S(2)-S(2)) is covalent and Cu-S is ionic. The cleave energy has a value between 0.1 and 1 J m^{-2}, and is used to identify the favored cleavage plane of a bulk surface. Smaller values are associated with the cleavage plane. This energy was calculated for the bulk surface of covellite along the (001) direction. The Cu(2)-S(1) bond has lower energy (γ = 0.30 J m^{-2}). Then, the Cu(2) acquires a trigonal planar geometry (Cu(1)-S(1)$_3$); this could be why the oxidation state of covellite is defined as Cu(I) [12–14].

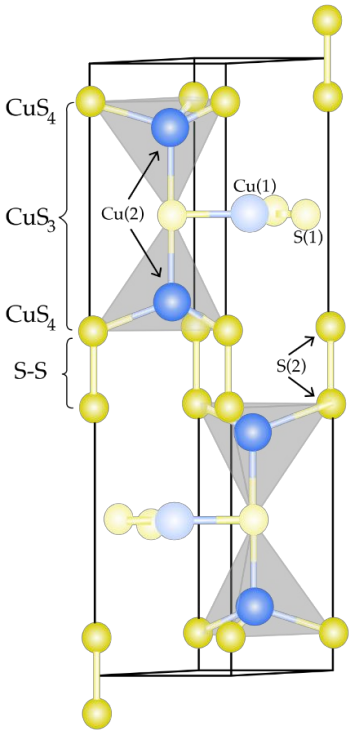

Fig. 1. Crystal structure of covellite. Spheres represent S(2) (dark yellow), S(1) (light yellow), Cu(2) (dark blue) and Cu(1) (light blue). (Adapted from [16]).

Xanthate and thionocarbamate collector types are widely employed in copper mining. The IPETC is considered a selective collector, offering a higher selectivity against iron sulfides such as pyrite, and high chemical stability in a wide range of pH due to its pK_a $\geq$ 12 [17]. The high selectivity is because the thionocarbamates do not form complexes with Fe^{2+} or Fe^{3+} in dilute aqueous solutions at pH 4.0 and 7.0. This is due to the low affinity of Fe^{3+} for ligands containing aliphatic nitrogen. As a result, this reagent gives excellent pyrite rejection [18]. Also, the low affinity of iron ions with thionocarbamates could be linked to the band gap of the copper and iron atoms. For instance, chalcopyrite has a narrow band gap making the back donation covalent bond stronger, while the pyrite has a broad band gap making the opposite manner [19].

Furthermore, the IPETC contains N and S functional groups for chelation, making it an effective collector in terms of copper recovery [20]. Another characteristic of IPETC is that the O-alkyl group present in its composition influences the hydrophobicity of the collector, while the N-alkyl group controls the degree of reactivity towards the copper surface, which is affected by steric

accessibility [21,22]. The electron-withdrawing substituents in N-alkyl groupings reduce the electrostatic effect and normal covalent bond, thereby reducing the reactive strength between sulfide minerals and collectors and improving the selectivity of collectors against iron sulfide minerals [19].

PAX belongs to the xanthate family, commonly utilized as a bulk collector due to its comparatively lower selectivity. It is usually used in the flotation process in the scavenger stage. PAX is prepared by reacting n-amyl alcohol, carbon disulfide, and potassium hydroxide. The carbon disulfide promotes the hydrophobicity of the collector, and the long alkyl chain increases its collecting power [22,23]. Even though IPETC and PAX have been commonly employed in mineral processing, some unresolved questions exist concerning the type of species adsorbed, its adsorption mechanism, and the relationship between species adsorbed and floatability.

Recently, some computational methods have been explored to study the interaction between collector molecules and mineral surfaces [19,24]. DFT is a helpful tool utilized to study the electronic structures of molecules and their electron density in order to understand the adsorption ability of the collectors on the mineral surface [24]. DFT has thus been used to study the adsorption mechanisms of different collectors on chalcopyrite. For instance, Zhao et al. [25] studied the collecting efficiency of two ether thionocarbamates, O-butoxy isopropyl-N-ethoxycarbonyl (BIPECTC) and O-(2-butoxy-1-methylethoxy) isopropyl-N-ethoxycarbonyl thionocarbamate (BMIPECTC), on chalcopyrite flotation. Using DFT, they performed frontier molecular orbital analysis, binding model simulation with copper ions, and molecular hydrophobicity analysis of each thionocarbamate. DFT calculations revealed that BMIPECTC has a higher reactivity and interacts strongly with copper compared to BIPECTC. Additionally, Ma et al. [22] studied the collector S-benzoyl O-isobutyl Xanthate (BIBX) in the selective flotation of chalcopyrite. They determined the chemical reactivity of the BIBX molecule using the concept of frontier orbitals (HOMO-LUMO), and found that the negative electrostatic potential is located on the C=S and C=O groups. Thus, the HOMO orbitals in BIBX were associated with sulfur atoms and the electron donor center of the BIBX (reactive sites in the molecule), and the presence of C=O in the BIBX increased the contribution of the LUMO orbital, thus increasing the scope for accepting electrons from copper. In another study by Liu et al. [25], the frontier molecular orbitals and the atomic charges were calculated to study the reactivity of thionocarbamates containing different N-substituent groups. The collectors studied were O-isobuthyl-N-ethyl-thionocarbamate (IBETC), O-isobuthyl-N-allyl-thionocarbamate (IBALTC), O-isobuthyl-N-acethyl-thionocarbamate (IBACTC) and O-isobuthyl-N-ethoxycarbonyl-thionocarbamate (IBECTC). The HOMO orbitals suggested that the order of electron-donating capacity was IBETC> IBALTC> IBACTC> IBECTC, and the LUMO orbital suggested that the order of electron-accepting capacity was IBACTC≈ IBECTC> IBALTC> IBETC. This result implies that IBACTC and IBECTC react with copper through a normal covalent bond and a π-backdonation covalent bond. They concluded that such behavior is a result of the ability of copper to form a stable six-membered complex with these collectors, making the IBECTC and IBACTC more efficient collectors of copper sulfide minerals than IBETC and IBALTC. These results show the relevance and significant contribution of the DFT when used as a complementary tool to study collector–mineral systems.

To the best of the author's knowledge, no studies have yet been published on the surface interactions between collectors and covellite, particularly with IPETC and PAX collectors. Therefore, this work presents FT-IR and XPS characterization techniques supported by DFT computational modeling to provide detailed information on the behavior of the collector–covellite system, followed by experimental validation.

2. Materials and methods

2.1 Materials

The mineral sample of covellite was obtained from a local Chilean mine. The covellite was associated with gypsum and quartz, as will be shown later (Section 3.1) via X-ray diffraction (XRD) characterization. The initial covellite samples were approximately 12 x 15 cm in size. The samples were crushed using a jaw crusher (BB 250XL) with a faw width of 120 x 90 mm and a gap width of setting 0-30 mm, until particles reached sizes below 1 cm. The covellite samples were further crushed by hand in an agate mortar for liberation, and were manually separated from the quartz and gypsum. The hand-picked covellite was dry-sieved to obtain different-size fractions. A coarse fraction (-2 mm +800 μm) was stored for use in the flotation test. Prior to each microflotation test, the necessary quantity of this fraction was grounded in an automatic agate mortar to obtain P_{80} = 100 μm.

The reagent employed for the microflotation and adsorption experiments was ultra-pure water (UPW), obtained using a MilliQ water purifier at a resistance of 18.2 MΩ. Sodium hydroxide (NaOH) of analytical grade was purchased from Ward's science and used to prepare an aqueous solution (0.01 M) as the pH regulator. IPETC and PAX were supplied by Qingdao Sunrun Chemical Co., Ltd. (China) at a nominal purity of ≥ 95 % and ≥ 90 %, respectively.

Finally, as mentioned, covellite was associated with gypsum. Therefore, to conduct the FT-IR and XPS characterization, it was necessary to wash the covellite to dissolve the gypsum present. Then, for each experiment, 1 g of covellite was placed in a beaker with 150 ml of ultra-pure water, stirred at 1000 rpm for 30 minutes, and filtered (this process was repeated twice). Then, the filtered mineral was dried at 40 °C in a vacuum oven for 24 hours.

2.2 Methods

2.2.1 Covellite characterization

The mineralogical phase of covellite was identified by X-ray diffraction (XRD) in a PANanalytical device, model XPERT PRO MPD Alpha 1, equipped with an X-ray source (Cu), monochromator (K-alpha) and detector (PIXcel1D, 45 kV, 40 mA). The analysis was performed in a 2θ range from 10° to 100° degrees. The morphological surface of covellite was characterized by scanning electron microscopy (SEM) with an EDS detector in a Hitachi Bruker detector, model SU5000, series 6. It was operated at 20 kV, taking images at 2500X using back-scattered electron (BSE) imaging. Microanalysis by X-ray dispersive spectroscopy (EDS) was performed to obtain the semiquantitative chemical composition. The adsorption was studied by FT-IR on a JASCO model FT-IR-4600, with a resolution of 0.7cm^{-1}, and ATR-IR accessory, in a spectral range of 4000–400 cm^{-1} using a germanium crystal for opaque minerals. XPS was used for the adsorption analysis in a Kratos Axos Ultra, with monochromatic Al Kα radiation and 20 eV pass energy. The binding energies were calibrated based on the C 1s peak (284.8 eV). Accurate curve-fitting analyses of the high-resolution Cu 2p, S 2p, O 1s, and C 1s were performed using CasaXPS software.

2.2.2 Microflotation test

Microflotation tests were carried out using a modified Hallimond-type flotation cell manufactured in-house (see Appendix A Fig. A1). The operational parameters were as follows: 150 mL cell volume, 1 g of covellite previously grounded with a size fraction of -74 +38 µm were used per test, N_2 = 33 mL/min nitrogen flow rate, and magnetic stirring between 1000 and 1200 rpm. The conditioning time was performed into a 200 ml beaker to ensure proper mixing. The conditioning time of 15 min was used for the collectors and 10 min for pH control. Afterward, the treated mineral was transferred into the Hallimond tube for flotation. The flotation time was 3 minutes. The pH values tested were 8, 9.5, and 11, controlled using a 0.01 M NaOH solution as the pH regulator. These pH values were selected because this pH range is typical in copper flotation operation. Three different collector concentrations were employed: 2×10^{-5}, $4 \times 10^{-5,}$ and 6×10^{-5} mol/L. The tests were performed in duplicate. Fig. 2 shows the flowsheet for the microflotation tests.

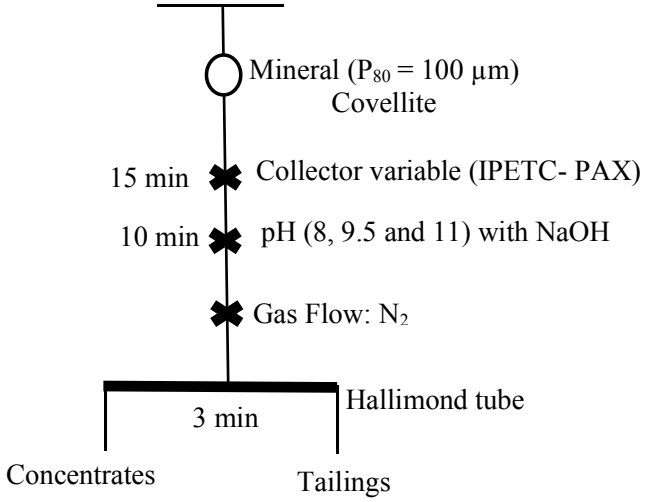

Fig. 2. Flowsheet of microflotation test using a modified Hallimond-type flotation cell.

2.2.3 Adsorption tests

Adsorption tests were carried out to study the chemical interaction between the covellite surface and each collector species. For the XPS analysis, 1 g of fine-fraction covellite (-53 µm) was added in ultrapure water and mixed with the collectors (IPETC and PAX) at a concentration of 1×10^{-3} mol/L at pH 8 and 11. After 30 minutes of stirring, the mineral slurry was washed once with ultrapure water, filtered, and dried at 40 °C in a vacuum oven for 24 h. The powder thus obtained was analyzed by XPS. The same adsorption procedure was employed for the FT-IR analysis, although in this case, the covellite particles were grounded in an automatic agate mortar to a particle size of ≤ 10 µm.

2.2.4 Computational methods

The geometries of collectors IPETC and PAX and their corresponding complexes with Cu(I) and Cu(II) cations were optimized using the DFT method [22,23], with the hybrid exchange–correlation

functional B3PW91[26] and the basis set 6-31g(d) [27,28], using Gaussian 09 computational chemistry software [29,30]. The Polarizable Continuum Model using the integral equation formalism variant [31] was adopted to calculate the properties of molecules in an aqueous solution. The binding model and molecular energy were calculated with the same basis set. The Avogadro package [32] was employed for drawing, and we pre-optimized the initial molecular structures through molecular mechanics using the Universal Force Field (UFF) [33].

3. Results and discussion

3.1 Covellite characterization

The XRD spectrum of the covellite sample is shown in Fig. 3. It shows crystalline covellite with the most intense peaks at (006), (103), (102), (110), (108), (116), (100), and (101). It showed an amorphous structure, with the peaks indexed in the graph with rhombus symbols [34]. The presence of gypsum was identified via the high peak position of 2θ = 12° and some less intense peaks between 20 and 25 degrees (circles). The composition of this mineral is 83% covellite and 17% gypsum.

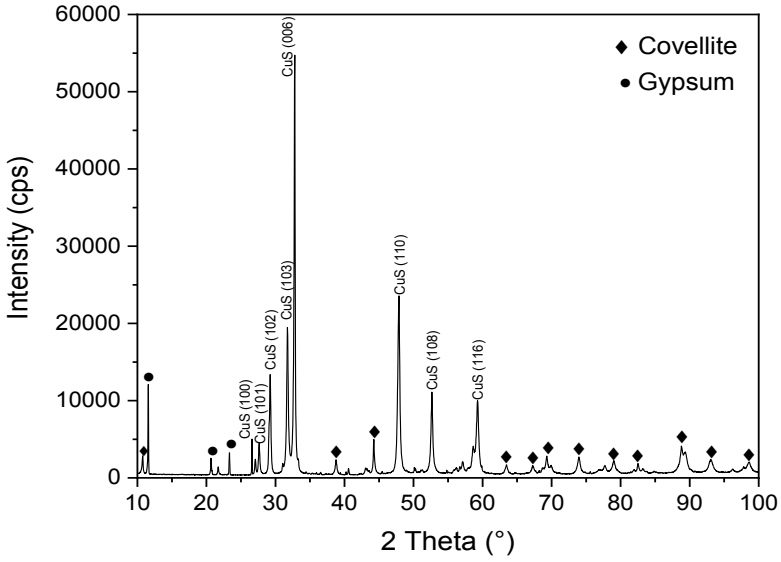

Fig. 3 X-ray diffraction pattern corresponding to covellite.

The morphology and different mineralogical phases are shown in Fig. 4a-g. Fig. 4a presents the EDS analysis of the covellite; the elements present were Cu (50.3%), Ca (4.3%), S(28.7%), Si(3.7%), and O (13%). Other mineral phases associated with covellite, such as $CaSO_4{\cdot}2H_2O$ and SiO_2, were also identified. These results corroborate the XRD findings, although SiO_2 was not recognized by the latter. This is perhaps due to the low SiO_2 concentration, below the limit of detection in XRD. Additionally, Fig. 4c-g depict elemental mapping, differentiating how the elements Cu, Ca, S, Si, and O are distributed. This analysis shows that even after the mineral preparation described in Section 2.1, the covellite used for microflotation testing had Ca- and Si-containing impurities.

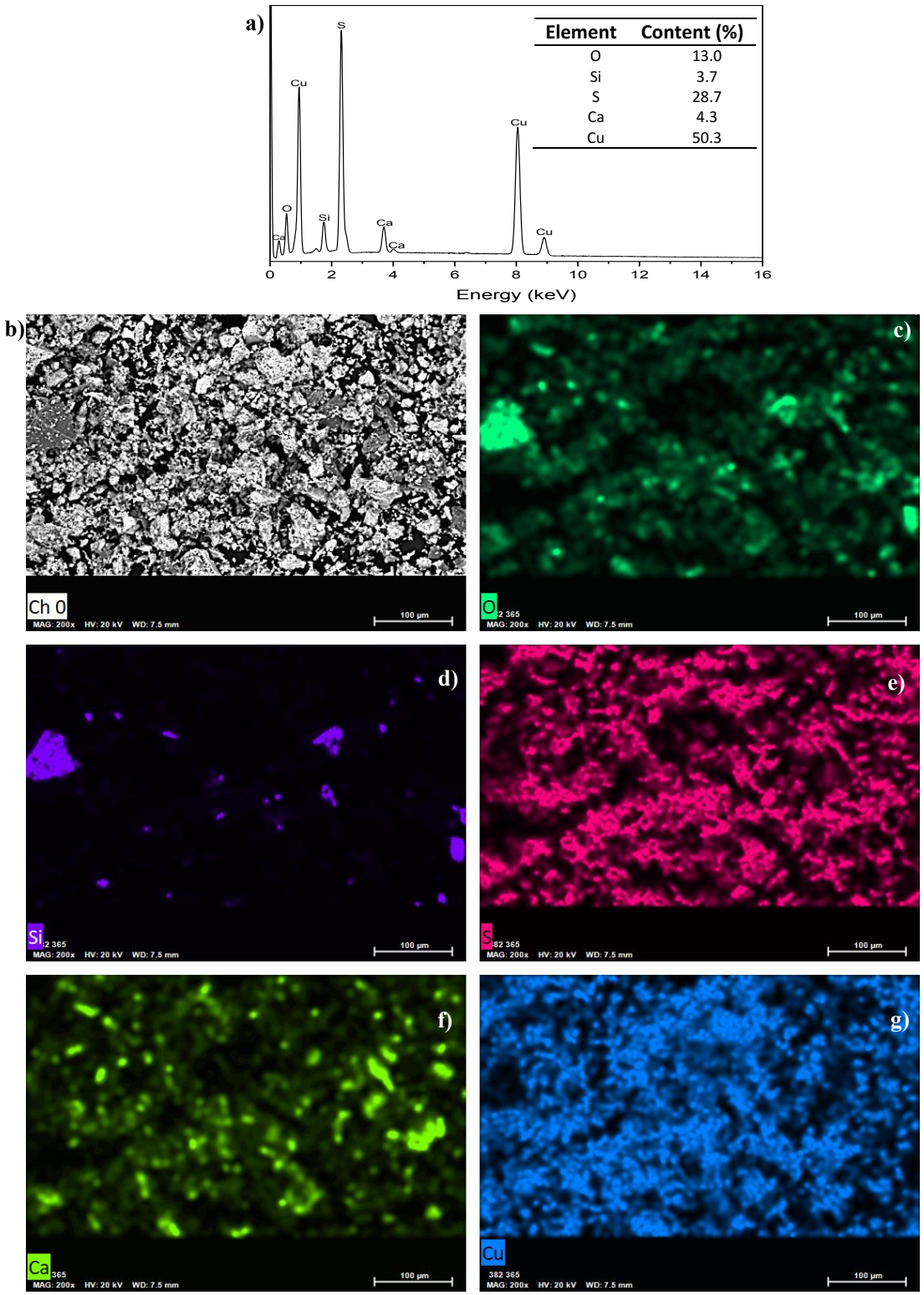

Fig. 4. SEM images of covellite: a) EDS elemental analysis; b) BSE covellite image; from c) to g) elemental mapping.

3.2 Microflotation test

First, covellite microflotation tests were carried out without a collector at pH 8, 9.5, and 11. The results indicate that the natural floatability of covellite is not pH-dependent in this range, with an average recovery of approximately 53 ± 2 %. Then, microflotation tests using collectors were performed at the same pH values and collector concentrations of 2×10^{-5}, 4×10^{-5}, and 6×10^{-5} mol/L. The collector had a marked effect on the covellite flotation, as the recovery increased to 88-93%. Additionally, covellite flotation was not pH-dependent. As seen in Table 1, the covellite recovery increased significantly with higher collector concentrations. At 6×10^{-5} mol/L of IPETC, for example, the recovery increased by 10% compared with 2×10^{-5} mol/L, while the difference in recovery using PAX was 13%.

Table 1. Covellite recovery (mean values and standard error) in microflotation tests without collector, covellite–IPETC, and covellite–PAX.

Collector concentration (mol/L)	**Covellite recovery (%)**			
	pH			
	8	**9.5**	**11**	**Average**
Non-collector	54 ± 2	51 ± 3	54 ± 1	53 ± 2
IPETC				
2×10^{-5}	78 ± 1	76 ± 2	79 ± 1	78 ± 2
4×10^{-5}	84 ± 1	85 ± 3	88 ± 3	86 ± 3
6×10^{-5}	89 ± 2	87 ± 3	87 ± 2	88 ± 2
PAX				
2×10^{-5}	75 ± 3	81 ± 1	83 ± 2	80 ± 4
4×10^{-5}	89 ± 3	88 ± 3	86 ± 1	88 ± 2
6×10^{-5}	93 ± 2	94 ± 2	93 ± 3	93 ± 2

These results show a clear interaction between the PAX and IPETC collectors and covellite surfaces. To better understand the nature of such interactions, FT-IR and XPS characterization supported by DFT computational modeling are presented in the following sections.

3.3 FT-IR characterization

Fig. 5 shows the FT-IR spectra for IPETC, covellite, washed covellite, covellite with IPETC at pH 8 (covellite+IPETC-8), and covellite with IPETC at pH 11 (covellite+IPETC-11), respectively. The IPETC spectrum shows a high frequency, resulting from the NH stretching vibration at 3278 cm^{-1}. Then, in the region 3000 to 2800 cm^{-1}, the bands correspond to the –C–H group (CH_3 at 2984 cm^{-1}, CH_2 at 2937 cm^{-1}, and CH_3 at 2875 cm^{-1}) [35]. The broad bands between 1700 and 1600 cm^{-1} correspond to the C=C group. The intense band at ~1520 cm^{-1} is due to –C(=S)–NH group vibration [17,35]. The bands at 1360-1300 cm^{-1} are attributable to CN stretching, NH deformation, and CH deformation. The peaks at 1176 and 1142 cm^{-1} correspond to COC and CNC asymmetric stretching, respectively [35]. Bands at 1230-1210 cm^{-1} are also present in the spectrum, corresponding to O–C=S asymmetric vibration, and 1110 cm^{-1} is attributed to O–C=S symmetric vibration [17]. The CN, C=S, and CH vibrations are represented by the 1100-1090 cm^{-1} bands. Finally, the C=S group is shown at 1050 cm^{-1}, and the C–S groups at 1050 and 725-590 cm^{-1} [36–39].

The covellite spectrum shows a band at 618.3 cm^{-1} corresponding to the stretching vibrations of Cu–S [13]. The presence of gypsum ($CaSO_4.2H_2O$) on the surface of covellite sample was again corroborated. Strong bands were observed at 1100 cm^{-1} and 696 cm^{-1}, associated with the tetrahedral group SO_4^{2-} of gypsum vibrations [40,41]. The washed covellite reveals a spectrum without the interference of gypsum. Here, the bands at 1100 cm^{-1} and 696 cm^{-1} disappear. These results could be explained based on the study executed by Yuan et al. [42], where the solubility of calcium sulfate dihydrate ($CaSO_4.2H_2O$) and the effect of NaOH solution was studied. At room temperature (20 °C), gypsum's solubility is 2.1 g/L. Since in our work 1 g of covellite (including ca. 17% gypsum) was used for the adsorption test, the total solubilization of gypsum would require 81 mL of water—a considerably lower volume than that used in the test (i.e., 150 mL). Another important aspect is the effect of NaOH on gypsum solubility. Yuan et al. [42] demonstrated that NaOH, in the concentration range utilized in our work, further increases the solubility of gypsum. Therefore, the formation of $Ca(OH)_2$ precipitate in the slurry is unlikely. This analysis suggests that the gypsum does not interfere with the adsorption of the collectors on the covellite surface.

As seen in Fig. 5, both the covellite+IPETC-8 and covellite+IPETC-11 spectra reflect IPETC adsorption on the covellite surface. Additionally, according to the Pourbaix diagram of covellite, in the pH range of 8-11, solid species Cu_2O and $Cu(OH)_2$ could be formed at potentials higher than zero (positive potentials) [43]. Nevertheless, the FT-IR shows no bands between 3650 and 3200 cm^{-1} corresponding to the OH group in both spectra. Therefore, the pulp potential could occur below this value, which is why the collector-adsorbed species on the covellite surface do not appear to be pH-dependent. A similar interaction between collector and covellite at this pH range would explain the results obtained in the microflotation tests (Section 3.2). The band at ~1590 cm^{-1} present in both spectra is due to the adsorption of –C(=S)–NH group vibration. The peaks at 3000 to 2800 cm^{-1} are bands of the –C–H group corresponding to the collector adsorbed onto covellite. The bands between 1360 and 1300 cm^{-1} are due to NH and CH deformation, the 1176 cm^{-1} band is due to COC, and 1142 cm^{-1} is related to the CNC of the adsorbed collector. Nevertheless, the characteristic NH stretching band (3278 cm^{-1}) of IPETC is absent from both spectra. The absence of this band could be due to the formation of Cu(IPETC') as a result of an anodic oxidation process involving the release of H^+ from the NH group (see Eq. 1). In Eq. 1, TC is a thionocarbamate, and TC' is a molecule without the hydrogen removed from the nitrogen atom [18,35]. Table 2 summarizes all the peaks indexed in the spectra.

$$Cu + TC \rightarrow Cu(TC') + H^+ + e^- \quad (1)$$

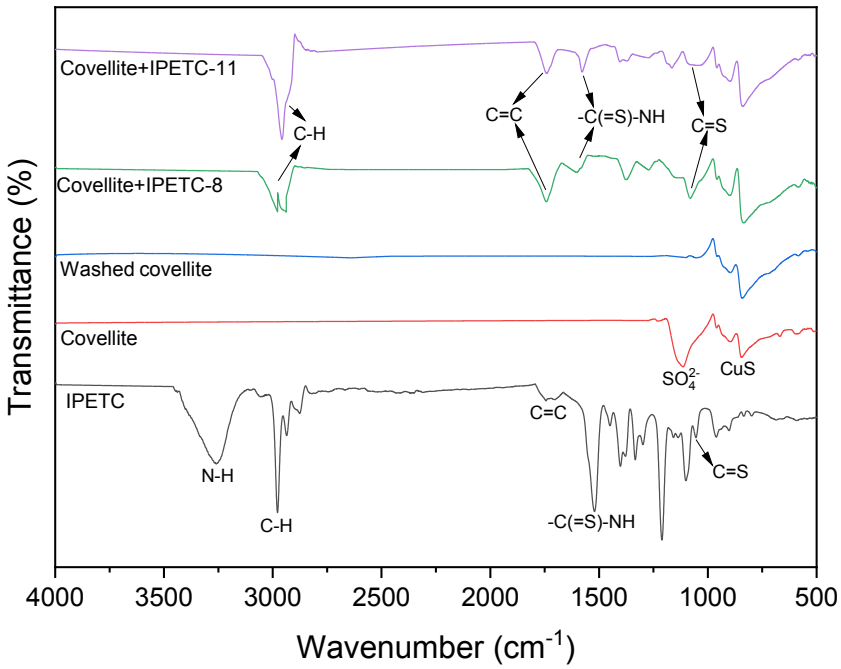

Fig. 5. Infrared spectra of covellite before and after treatment with IPETC at pH 8 and 11.

Fig. 6 exhibits the FT-IR spectra for PAX, covellite, washed covellite, covellite with PAX at pH 8 (covellite+PAX-8), and covellite with PAX at pH 11 (covellite+PAX-11), respectively. The PAX spectrum is in the region between 3000 and 2800 cm^{-1}, with bands corresponding to the –C–H group (CH_3 at 2984 cm^{-1}, CH_2 at 2937 cm^{-1}, and CH_3 at 2875 cm^{-1}) [35,39]. The band at 1750 cm^{-1} corresponds to C=O binding (bind type ketone/ aldehyde; this bind is characteristic of PAX because one of the reagents used to prepare the PAX is n-amyl alcohol). The bands at 1490-1000 cm^{-1} and the intense band at 1070 cm^{-1} correspond to C=S vibration (carbon disulfide) [44,45]. The covellite and washed covellite spectra show the same gypsum solubilization behavior as was aforementioned.

The covellite+PAX-8 and covellite+PAX-11 spectra show PAX adsorption on the covellite surface. Additionally, the collector adsorption on the covellite surface is not pH-dependent for both spectra, as was explained before for the IPETC. This confirms the result obtained in the microflotation test, and the same behavior is shown for IPETC. The region between 3000 and 2800 cm^{-1} present in both spectra is related to the adsorption of –C–H group vibration, while 1750 cm^{-1} corresponds to C=O adsorption. The region between 1400 and 1000 cm^{-1} refers to several interactions between covellite and PAX. To better identify these bands, the right side of Fig. 6 shows a closer view of this region so as to show the species formed more clearly. The enhanced area presents the frequencies for the PAX, Cu-amylxanthate (CuAX) and dixantogen $(AX)_2$ formed. Under COC stretching vibration, $(AX)_2$ was identified in the bands at 1367-1290 cm^{-1}, 1242-1239 cm^{-1}, 1150 cm^{-1}, and 1109-1108 cm^{-1}. CuAX was identified at 1190-1189 cm^{-1} and 1125 cm^{-1}. PAX appeared at 1173 cm^{-1} and 1100 cm^{-1}. Under C=S stretching vibration, the $(AX)_2$ was identified at 1025 cm^{-1} and the PAX was identified at 1052-1049 cm^{-1} [46,47]. Table 2 summarizes all the peaks indexed in the spectra.

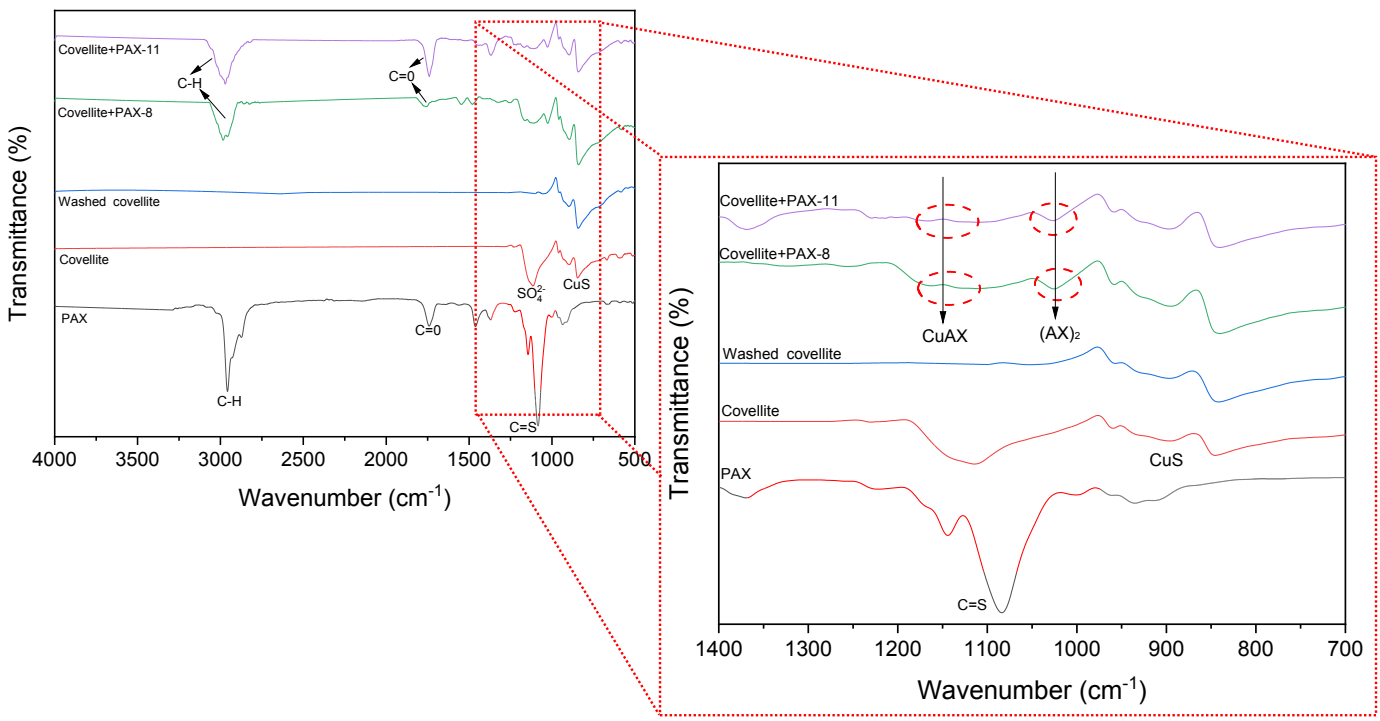

Fig. 6. Infrared spectra of covellite before and after treatment with PAX at pH 8 and 11. Enhanced image shows Cu-amylxanthate (CuAX) and dixantogen $(AX)_2$.

Therefore, the active hydrophobic species on the covellite surface responsible for covellite flotation are the metal xanthate (MX) and the dixantogen (X_2). The formation of these two species could be due to the solubility of the covellite, which at pH 5.3 is 4×10^{-3} mol/L. This solubility is high compared to the solubility of other copper sulfides such as chalcopyrite (3.3×10^{-4} mol/L.) and chalcocite (2.6×10^{-5} mol/L). Thus, these solubilized ions can cause the rapid oxidation of xanthate to dixanthogen. So, large quantities of X_2 from the PAX in the solution are formed, which could then co-adsorb with the MX on the covellite surface and reinforce collection. The adsorption mechanism could be through the electron-donating (reducing reaction) of PAX and chemisorption onto covellite surface. Therefore, the PAX is a reducing agent [7,18].

Table 2. The peak position of FT-IR obtained for covellite, washed covellite, covellite –IPETC, and covellite–PAX

	Functional group	Initial peak position (cm^{-1})	Final peak position (cm^{-1})	Reference
Covellite	Cu–S	618.3		[13]
	SO_4^{2-}	1100 and 696		[41,42]
Washed covellite	Cu–S	618.3		[13]
	SO_4^{2-}	absent		
IPETC	NH	3270		[36]
	CH_3	2984		
	CH_2	2937		

	CH_3	2875		
	C=C	1700-1600		[17,36]
	–C(=S)–NH	~ 1520		
	CN, NH and CH	1360-1300		
	COC (asym)	1176		
	CNC (asym)	1142		
	O–C=S (asym)	1230-1210		
	O–C=S (sym)	1110		
	CN, C=S and CH	1100-1090		
	C=S	1050		[37–40]
	C–S	725-590		
Covellite+IPETC-8 and Covellite+IPETC-11	–C(=S)–NH		~1590	[20,36]
	–CH		3000-2000	
	NH, CH		1360-1300	
	COC		1176	
	CNC		1142	
	NH		absent	
PAX	CH_3	2984		[36,40]
	CH_2	2937		
	CH_3	2875		
	C=O	1750		
	C=S	1490-1000, 1070		[44,45]
Covellite+PAX-8 and Covellite+PAX-11	–CH		3000-2800	[47,48]
	C=O		1750	
	(Vibracional mode COC):			
	$(AX)_2$		1367-1290, 1242-1239, 1150	
	CuAX		1190-1189, 1125	
	PAX		1173-1100	
	(Vibracional mode C=S):			
	$(AX)_2$		1025	
	PAX		1052-1049	

3.4 XPS characterization

XPS measurements were performed to determine the surface composition of the covellite and its oxidation state, as well as to investigate the adsorption mechanism of the collectors IPETC and PAX on the covellite surface. According to the XRD and FT-IR results detailed in sections 3.1 and 3.3, the covellite samples have traces of gypsum. Therefore, two samples were analyzed—covellite and washed covellite—to see if the gypsum was solubilized or if this specie influences covellite's behavior when interacting with collectors.

Fig. 7 presents the high-resolution XPS spectra of Cu 2p, S 2p, O 1s, and C 1s in covellite and washed covellite. The Cu 2p spectrum shows the leading peaks of covellite. A single sharp peak at 932.14 eV could be due to CuS(I). The binding energy position at 933.12 eV may be related

to the CuS(II). This signal is accompanied of characteristics satellites that are located in the energy range of 944-941 eV, these are the signature of Cu(II) [35,49]. Also, the peak located at 934.65 eV may be attributed to the $Cu(OH)_2$. The lower intense peak at 936.04 could be associated with $CuSO_4$ [48–50]. These results demonstrate that although Cu(I) has been typically considered the main oxidation state of covellite, the covellite remains with the oxidation state of Cu(II) [35,51]. Nevertheless, once the covellite was washed, its spectrum was shifted to the right at a lower binding energy (see Cu 2p spectrum). The shift at lower binding energy may be related to the change of the local environment of Cu(I) atoms upon crystallization of the copper sulfide [35,52–54]. Finally, these results suggest that covellite is comprised of copper ions with mixed-valence states of +1 and +2 [15,35,51].

The S 2p spectrum of covellite presents two main doublets. The minor doublet could be fitted at 161.28 eV, related to sulfide (S^{2-}), and a predominant doublet at a binding energy of 162.18 eV associated with disulfide (S_2^{2-}). A third doublet located at 163.3 eV may be related to nonstoichiometric sulfides (S_x^{2-}) or elemental sulfur (S°) [55], while the peak located at 169.6 eV may be related to sulfides derived from gypsum (SO_4^{2-}) [15,50,56]. The washed covellite spectrum present the peaks associated with sulfide (S^{2-}) at 161.27 eV and disulfide (S_2^{2-}) at 162.23 eV both of them characteristic of the covellite structure [35,52,57]. Here, it is corroborated that the gypsum was solubilized because the peak around 169.6 eV disappeared.

The O 1s spectrum of covellite shows a peak at 531.54, which may be related to $metal(OH)_x$ ($Cu(OH)_2$). Additionally, the intense peak located at 532.54 may be related to SO_4^{2-}. This species could be due to the covellite oxidation or the gypsum present in the covellite. The signal between 533 and 534 eV may be due to the adsorbed H_2O at the surface. The washed covellite spectrum shows a peak related to copper oxide at 529.68 associated with CuO. Also, the intensity of peaks related to the water in washed covellite are higher than covellite [35,50,51,54,58].

The C 1s spectra show that the covellite and washed covellite have the same peaks, and both of them have been exposed to the atmosphere, as we detected adventitious carbon contamination at 284.7 eV. Also, the C-H was identified at 282.30 related to the carbide [52–54]. Table 3 displays the binding energies of each species formed.

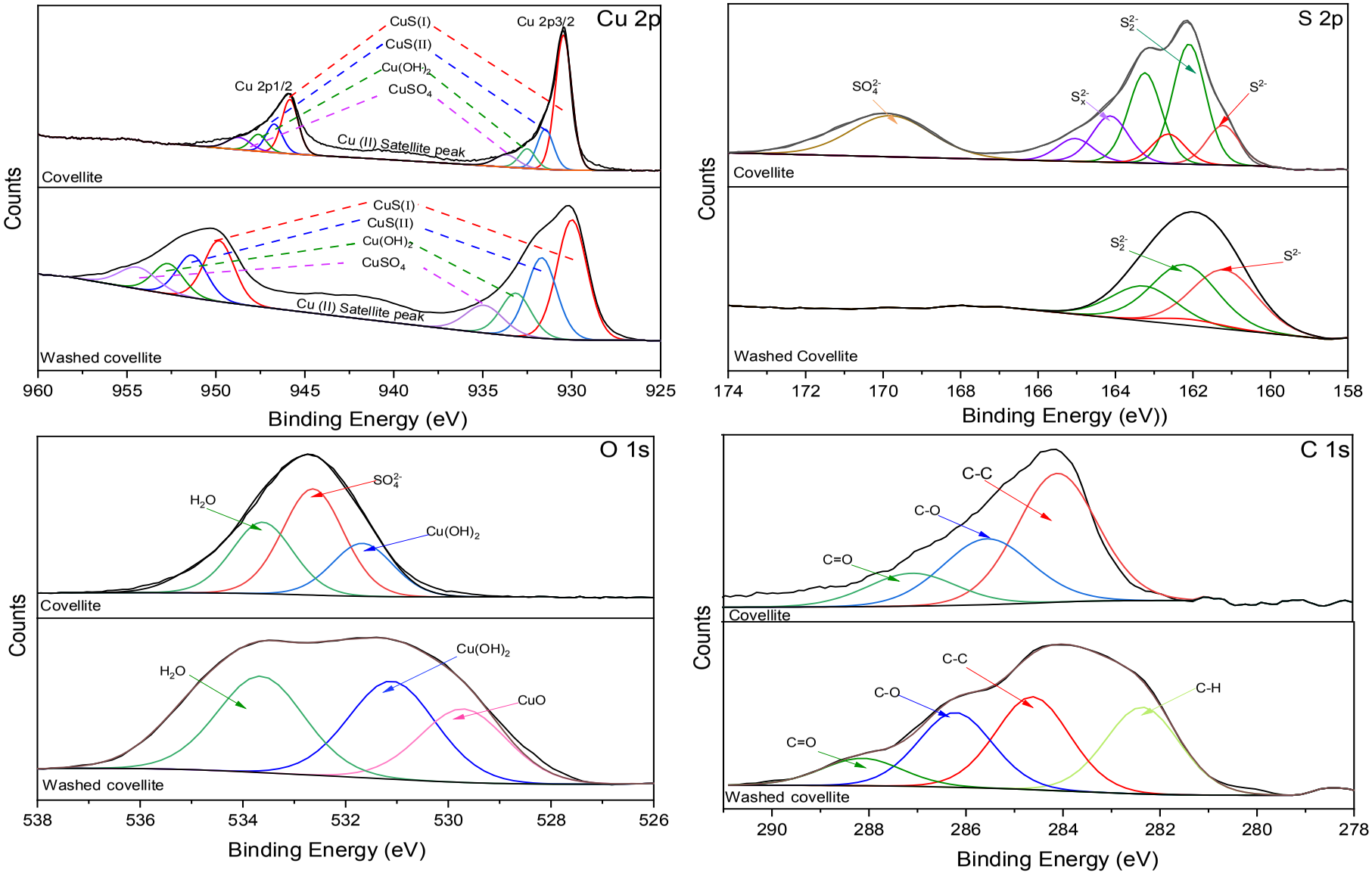

Fig. 7. Cu 2p, S 2p, O 1s, and C 1s XPS spectra recorded on the surface of covellite and washed covellite.

Fig. 8 presents the high-resolution XPS spectra of Cu 2p, S 2p, O 1s, and C 1s of washed covellite, covellite treated with PAX (PAX-11), and covellite treated with IPETC (IPETC-11). A collector adsorption test was performed with each collector at pH 8 and 11. The results show no relevant difference between the behaviors of covellite with PAX at pH 8 and pH 11. This could be because the intensity of metal-hydroxide ($Cu(OH)_2$) and CuO are not relevant in the spectrum O 1s at 531.40 and 529.68 eV, respectively. It is worth mentioning that the scale of this spectrum was maximized to enlarge the spectrum and better identify the species. The same behavior was observed for IPETC (see Appendix A Fig. A2-A6). Therefore, XPS analysis was carried out with PAX and IPETC at pH 11. The spectrum of washed covellite was used to analyze the adsorption mechanism of each collector on the covellite surface. The atomic concentrations of Cu 2p, S 2p, O 1s, and C 1s of washed covellite, covellite treated with PAX, and covellite treated with IPETC are given in Table A1 (see Appendix A). The S to Cu atomic concentration ratio was 1.0, according to the stoichiometry of covellite. The increase in the atomic concentrations of C 1s and S 2p confirms the adsorption of PAX on the covellite's surface. The increase in the atomic concentrations of Cu 2p, S 2p, and C 1s confirms the adsorption of IPETC on the covellite's surface. Additionally, these results show that most of the calcium belonging to gypsum was solubilized.

The mechanism of adsorption of PAX on the covellite surface is principally through Cu 2p, C 1s, and S 2p. The Cu 2p spectrum shows a single sharp peak at 932.2 eV, this signal may be related to the CuS(I) and a minor peak at 933.6 eV may be related to Cu(II). Besides, the absence of the satellites peaks of Cu(II) corroborated that the oxidation state of covellite with PAX is Cu(I). These results confirm that the xanthates are reducing agents because the Cu(II) was reduced to Cu(I) [18]. This finding was corroborated by FT-IR by the identification of Cu-amylxanthate (CuAX) and dixantogen $(AX)_2$ on the covellite surface. The C 1s of washed covellite has an atomic concentration of 15.52%. Then, after treatment with PAX, the atomic concentration of C 1s is 48.6%. These results reveal that Cu atoms can be bonded to the –C site through C–S and C=S groups (see Appendix A Table A1). Additionally, the S 2p spectrum shows a well-defined doublet at 162.0 eV related to S_2^{2-}. This result suggests that the interaction between PAX with covellite surface is stronger through the disulfide rather than monosulfide [20,21,53]. Also, it was corroborated that the gypsum was solubilized because the peak around 169 eV disappeared. Thus, this species does not interfere with the collector adsorption.

The adsorption mechanism of IPETC on the covellite surface could be explained via the atomic concentrations of Cu 2p and S 2p, which increase once the covellite is treated with IPETC (see Appendix A Table A1). This suggests the bind is facilitated by the S of the collector with Cu atoms on the covellite surface. Moreover, the S 2p spectrum of covellite treated with IPETC displays a principal doublet at 162.18 eV attributed to S_2^{2-} (C=S functional group), as observed for thiourea. Then, at 161.28 eV, we find the peak characteristic of covellite, which is S^{2-}, and the minor doublet at 164.18 eV could be attributed related to elemental sulfur (S°) or nonstoichiometric sulfides (S_x^{2-}). The peak at 169.46 eV is attributed to SO_4^{2-}, which could be related to the gypsum [20]. The Cu 2p spectrum shows a single sharp peak at 932.3 eV related to the CuS(I), also a peak at 933.50 eV attributed to the CuS(II), this signal is accompanied by the characteristic satellites that are located in the range 944-941 eV, signature of the Cu(II) [35]. Also, the peak at 934.50 related to $Cu(OH_2)$ was identify [58]. The NH functional group was not identified by XPS characterization (the N 1s spectrum did not show any signal). Finally, we see slight adsorption of IPETC by O 1s and C 1s (the scale of this spectrum was maximized to enlarge the spectrum and better identify the species), which could be negligible. Table 3 summarizes all the binding energies peaks indexed in the spectra.

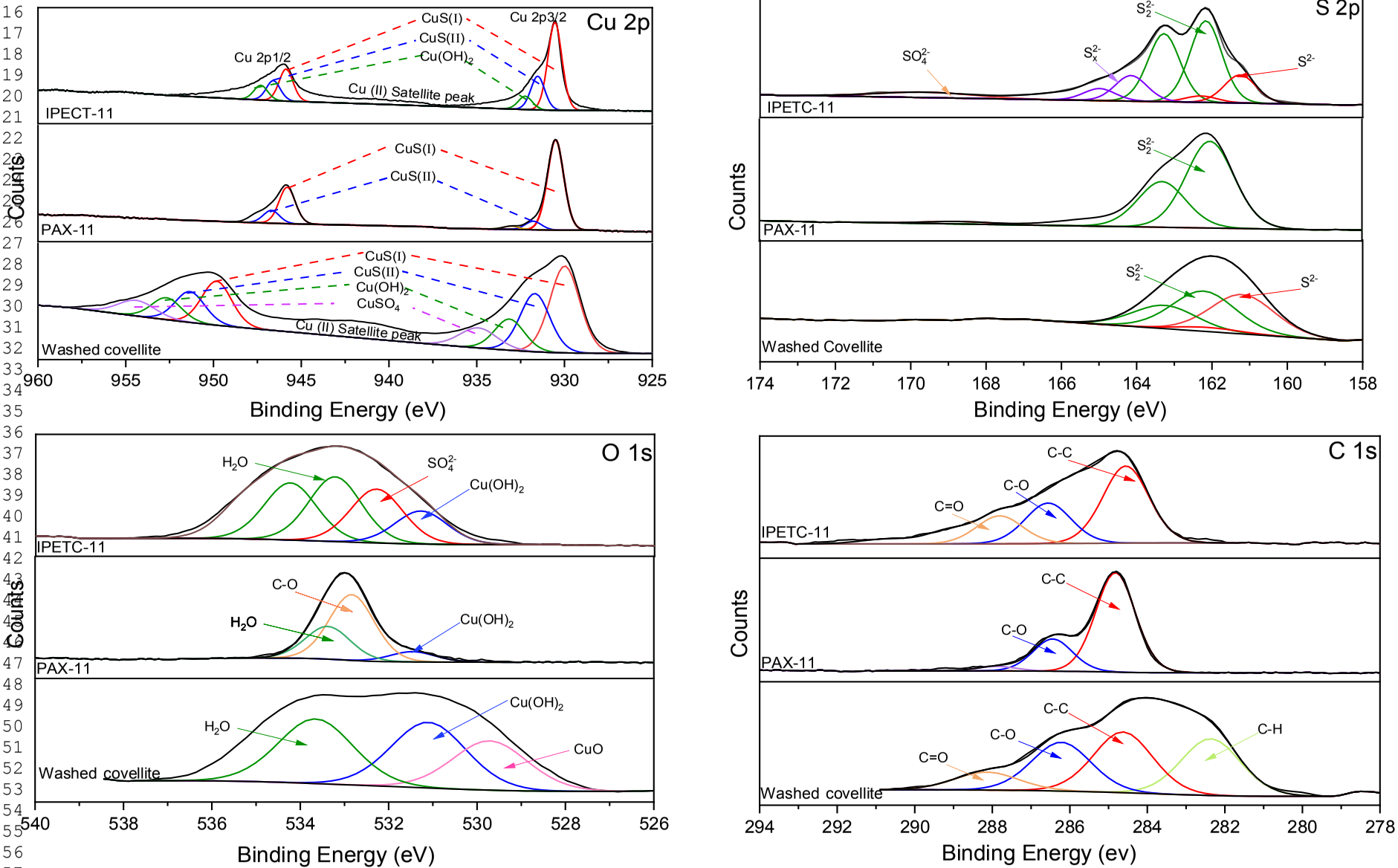

Fig. 8. Cu 2p, S 2p, O 1s and C 1s XPS spectra recorded on the surface of washed covellite, covellite treated with PAX and IPETC at pH 11.

Table 3. Binding energies (BE) position of the leading peaks in the Cu 2p, S2p, O1s and C1s high resolution spectra obtained for covellite, washed covellite, IPETC-11 and PAX-11

Sample	Cu 2p (eV)		S 2p (eV)		O 1s (eV)		C 1s (eV)	
	Specie	Peak position	Specie	Peak position	Specie	Peak position	Specie	Peak position
Covellite	CuS(I)	932.14	S^{2-}	161.28	$Cu(OH)_2$	531.54	C-C	284.70
	CuS(II)	933.12	S_2^{2-}	162.18	SO_4^{2-}	532.54	C-O	286.00
	$Cu(OH)_2$	934.65	S_x^{2-}	163.30	H_2O	533.64	C=O	287.60
	$CuSO_4$	936.04	SO_4^{2-}	169.60				
	Cu(II) satellite	941-944						
Washed covellite	CuS(I)	930.65	S^{2-}	161.27	CuO	529.68	C-H	282.50
	CuS(II)	931.70	S_2^{2-}	162.23	$Cu(OH)_2$	531.40	C-C	284.80
	Cu_2O	933.17	S_x^{2-}	absent	H_2O	533.70	C-O	286.29
	$CuO/CuSO_4$	935.00	SO_4^{2-}	absent			C=O	288.20
	Cu(II) satellite	941-944						
IPETC-11	CuS(I)	932.30	S^{2-}	161.28	$Cu(OH)_2$	531.38	C-C	284.70
	CuS(II)	933.50	S_2^{2-}	162.18	SO_4^{2-}	532.28	C-O	287.80
	$Cu(OH)_2$	934.50	S_x^{2-}	164.18	H_2O	533.29	C=O	286.60
			SO_4^{2-}	169.46	H_2O	534.32		
PAX-11	CuS(I)	932.20	S_2^{2-}	162.00	$Cu(OH)_2$	531.5	C-C	284.80
	CuS(I)	933.6			C-O	533.0	C-O	286.60
					H_2O	533.5		

3.5 Molecular modeling

It is possible to identify points of activity in the collectors' structures that optimize their molecular geometry and calculate the molecular electrostatic potential to predict the reactive sites of collectors (positive, negative, or neutral electrostatic potential). Moreover, the frontier molecular orbital (FMO) can be determined via the highest occupied molecular orbital (HOMO) and lowest unoccupied molecular orbital (LUMO), which reflect the donor and receptor capacity of the collector, respectively. HOMO is the electron donor, and LUMO is the electron acceptor. The smallest energy gap between HOMO and LUMO ($\Delta E_{HOMO-LUMO}$) means that the chemical reactivity here is strongest (less stable), which increases the ability of the collector to interact with the mineral surface [54,55]. Additionally, the HOMO–LUMO orbitals allow for calculating the global reactivity descriptors using DFT calculations. The global reactivity descriptors are electrophilicity (ω), which determines the system's chemical reactivity, and electrochemical potential (μ), which describes the charge transfer within a system. Compounds with greater μ are more reactive than those with a low μ. The hardness (η) and softness (S) are related to the HOMO–LUMO energy gap. When the HOMO–LUMO energy gap is high, the molecule is more stable and chemically harder than molecules with a small HOMO–LUMO energy gap. The last descriptor is electronegativity (χ), which measures the molecule's ability to attract electrons to itself [54,56–59]. Additionally, the binding model predicts the bonds formed between the actives sites of the collector and mineral surface. This analysis can be performed using the Wiberg bond index, which is extensively used as a bond analyzer. This binding model serves to compare the binding ability of collectors and copper ions. Finally, the atomic charges can be calculated using natural bond orbital (NBO) analysis, which describes the reactivity of the molecules.

3.5.1 Molecular electrostatic potential and NBO analysis

The optimized molecular geometries of $IPETC^-$ and PAX^- in water are shown in Fig. 9a and 9b, respectively. The leading elements of the $IPETC^-$ structure are labeled C1, N3, O2, and S4, and those of PAX^- are C2, O1, S3, and S4, the last of which corresponds to =S (see Fig. 9 a and 9b). Table 4 presents the NBO atomic charges. Here, it can be seen that when IPETC is ionized, the NBO net charge of S4 increases from -0.37 (IPETC) to -0.65 ($IPETC^-$), showing that the S4 in $IPETC^-$ has greater electronegativity, and, therefore, a greater ability to attract electrons. For C1, N3, and O2, there was no significant change in electronegativity. This result confirms the hypothesis mentioned in Section 3.3 that IPETC interacts via an anodic oxidation process. Additionally, in Fig. 9a, the molecular electrostatic potential (MEP) describes the electron density of the $IPETC^-$ molecule. The red coloration marks the most negative region (electrophile) and yellow the most positive region (nucleophile). Therefore, the MEP and NBO charges predict that the reactive site in the $IPETC^-$ is in the S4 element (C=S group). When PAX is ionized to PAX^-, there is no significant change in electronegativity (see Table 4). O1, S3, and S4 are the electronegative sites of PAX^-. The MEP of PAX^- shows that the most negative region is between S3 and S4, predicting that S3 (C–S group) and S4 (C=S group) are the reactive sites in the PAX^- molecule (see Fig. 9b). For C2 and O2, there was no significant change in electronegativity. These results agree with those obtained via XPS analysis. The XPS result for $IPETC^-$ suggests the binding is enabled by the S of the collector with Cu atoms in the covellite surface. In the case of PAX^-, it was also determined that the principle mechanism of adsorption of PAX^- on the covellite surface is through C 1s and S 2p (see Fig. 8).

a)

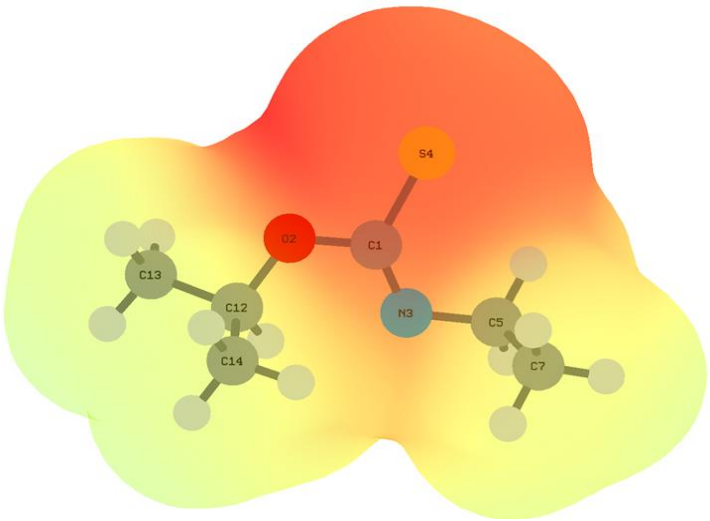

b)

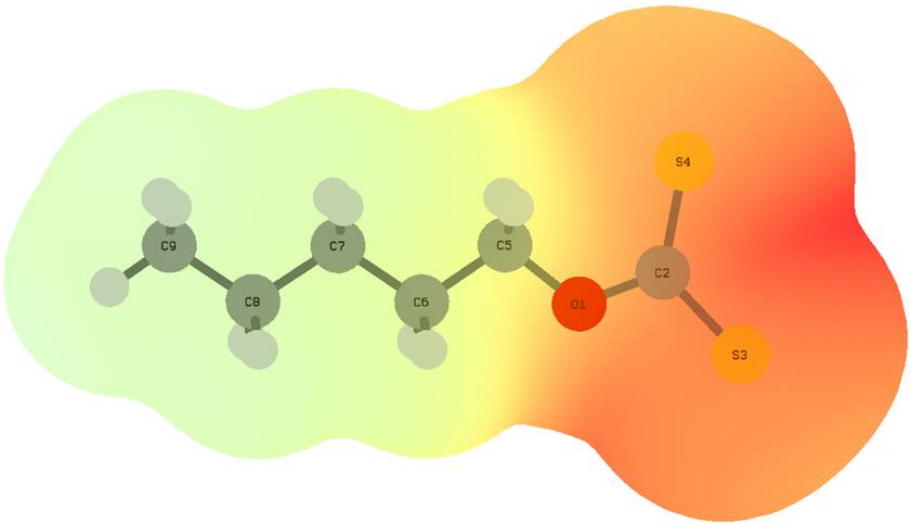

Fig 9. Molecular electrostatic potential of a) $IPETC^-$ and b) PAX^-

Table 4. NBO net atomic charges of IPETC and PAX molecules

Element	IPETC	$IPETC^-$	Element	PAX	PAX^-
C1	+0.44	+0.41	C2	+0.02	+0.00
O2	-0.53	-0.58	O1	-0.52	-0.53
N3	-0.62	-0.64	S3	-0.42	-0.42
S4	-0.37	-0.65	S4	-0.39	-0.39

3.5.2 Frontier molecular orbitals analysis

The global reactivity descriptors are widely employed to explain the electronic properties of compounds, and Table 5 presents the values for $IPETC^-$ and PAX^-. A high hardness (η) and low electrophilicity (ω) give a low reactivity. Therefore, the $IPETC^-$ has lower reactivity than PAX^- (see Table 5). Another descriptor is the electronic chemical potential (μ) associated with molecular stability. When μ is higher, the molecule is more reactive. Therefore, the absolute value of μ shows that $IPETC^-$ is more stable (less reactive) than PAX^-. The same behavior was identified in the HOMO–LUMO energy gap. A higher energy gap means a lower reactivity and, therefore high stability, demonstrating that $IPETC^-$ is less reactive. The PAX^- has greater electronegativity (χ) and a high charge flow, showing its higher reactivity. Finally, the softness (s) is the inverse of hardness and corroborates this behavior [60–65].

In conclusion, it is well known that the PAX^- is a type of xanthate collector, and xanthates have a powerful collector ability. This fact could explain the low stability of PAX^-. Nevertheless, these collectors have disadvantages, including ease of decomposition and poor selectivity. The latter is a disadvantage if selective separation is required in the first stage of the flotation process. Finally, the $IPETC^-$ calculations demonstrate that it has the highest stability, and, for this reason, it is generally a less potent collector than xanthates. Nevertheless, the advantage of using $IPETC^-$ is its solution stability due to having a pKa ≥ 12. The pKa of a collector influences the mechanism of collector

adsorption on the mineral surface, and can be a critical factor in determining optimum flotation conditions [17]. Finally, these results support using PAX^- as a bulk collector and $IPETC^-$ as a selective collector in the flotation process.

Table 5. Global reactivity descriptors calculated for $IPETC^-$ and PAX^-

	HOMO (eV)	LUMO (eV)	ΔE (eV)	μ (eV)	η (eV)	s (1/eV)	χ (eV)	ω (eV)
$(IPETC)^-$	-0.1854	0.0555	6.5536	-1.7674	3.2768	0.1526	1.7674	0.4766
$(PAX)^-$	-0.1878	-0.0209	4.5405	-2.8398	2.2703	0.2202	2.8398	1.7761

3.5.3 Binding model

The binding model between the collector $IPETC^-$ and PAX^- with covellite was simulated. The structural geometries of the collector were optimized using two copper cations, Cu(I) and Cu(II). The two oxidation states of copper were used because they are shared by the covellite structure, and they could interact differently with the collectors [12,14,16,65]. Nevertheless, the optimized structures of $IPETC^-$ with Cu(I) and Cu(II) cations do not exhibit any difference related to copper's binding with $IPETC^-$. In both cases, Cu(I) and Cu(II) were bonded with the S4 element (see Fig. 10a). However, the NBO net charges of the elements O2, N3, and S4 of the collector change when the copper ion changes from Cu(I) to Cu(II), demonstrating significant differences between the interactions of these cations with $IPETC^-$. The PAX^- presents the same behavior. There is no difference between Cu(I) and Cu(II) binding with PAX^-; in both cases, the copper ions Cu(I) and Cu(II) bond with S3 and S4 of the PAX^- molecule (see Fig. 10b). Finally, similar to $IPETC^-$, the NBO net charges of the O1, S3, and S4 elements of PAX^- are different.

a)

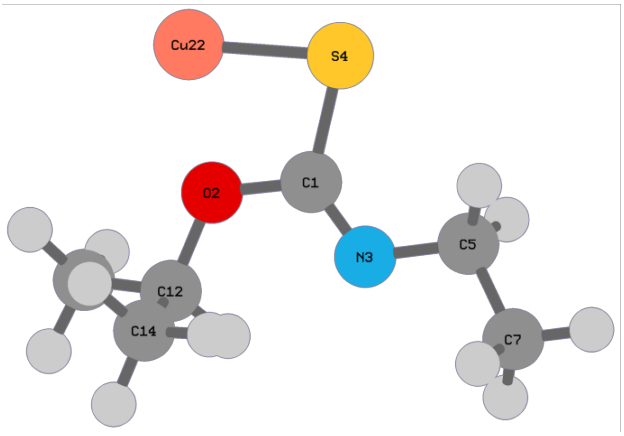

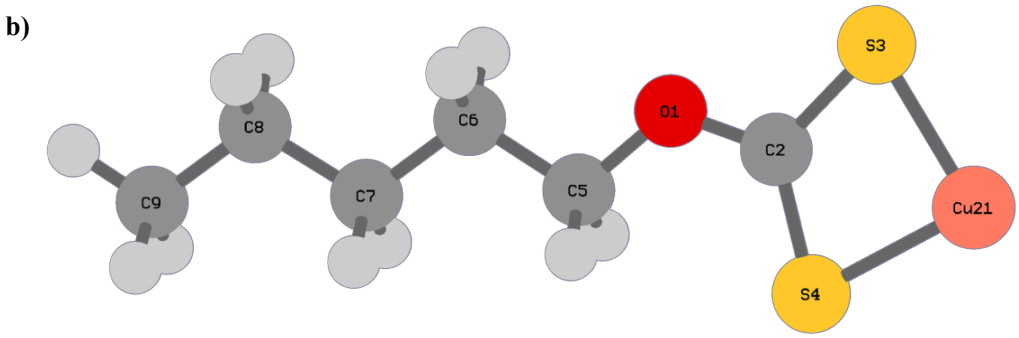

Fig 10. Optimized geometries of the binding models of a) copper–IPETC$^-$ and b) copper–PAX$^-$

Besides, the DFT calculations verified that it is less probable to form a stable bond Cu-O. Indeed, as was shown in Fig. 9, section 3.5.1, in the molecular electrostatic potential maps, the negative charges were mainly located on the C=S group, and the most negative atom charge is on S atom (-0.65) compared with O atom (-0.58). Also, the results showed in Fig. 11 suggest that IPETC- Homo orbitals are centered at the C=S group, which indicated that C=S group might be the electron-donating site in the interaction. The same behavior was observed for Homo orbitals in the PAX- with terminals on S atoms. Similar behavior was demonstrated by Zhao et al. 2016 [66] calculating the binding model between copper ion (II) and IPETC using DFT. They demonstrated that the bond only occurs through the C=S group, while the C=S and C=O groups are both involved in other kinds of thionocarbamates, which contain different N-alkyl and O-alkyl groups such as IBECT, BIPECTC, and BMIPECTC.

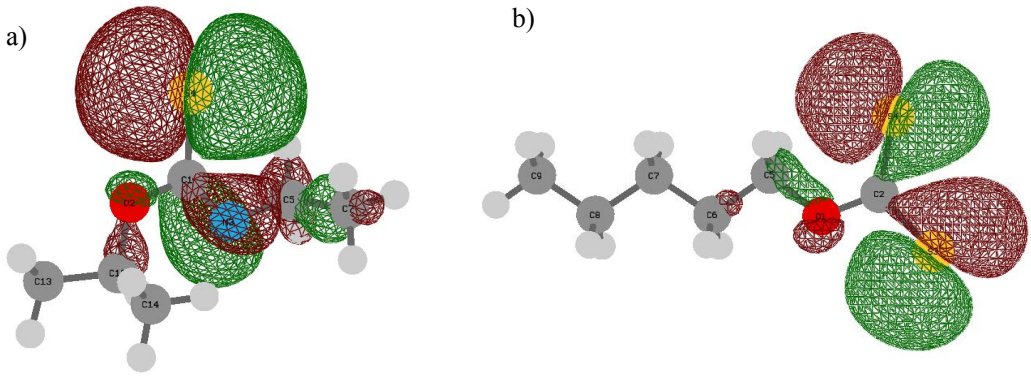

Fig 11. Homo orbitals for collectors (a) IPETC-, (b) PAX-. Red and green mean positive and negative values of the wavefunction, respectively.

It is worth mentioning that we decided to conduct the DFT calculations using the metal ions rather than periodic mineral crystal planes because the collector reactivity with a metal ion has been extensively studied, demonstrating that the collecting ability of collector on metal ions could be analyzed using this method [66]. For instance, Bag et al.[67] studied the predictive capacity for geometrical optimization of xanthates with copper ions. Also, they carried out a flotation test to

support their findings. The DFT calculations showed the interaction between various alkali-xanthates and copper ions. The results indicate that amyl-xanthate is most effective compared to ethyl, propyl-, iso-propyl, butyl- and iso-butyl xanthate. Then, from the flotation using the batch flotation technique, the experimental results show that better values of copper recovery were obtained with amyl-xanthate rather than other xanthates, supporting DFT calculations. Another work was conducted by Zhao et al.[68]. They studied the binding model of two hydroxamic acids (BHA and CHA) with Ca(II) ion through DFT calculations. They demonstrated that in alkaline solutions, the dianion of CHA exhibited higher atomic charge value and HOMO energy, bigger dipole moment, and binding energy with Ca(II), and hence stronger collecting ability for scheelite ($CaWO_4$) than those of BHA. These results agreed with experimental results obtained from the flotation tests, zeta potential, and the determination of adsorption quantity.

Yekeler and Yekeler [68] conduct the DFT calculations to model the interactions between thiol collectors with Ag (I) ion, and optimize the geometries of collector–Ag complexes formed. The results showed that the optimized geometries agree with the experimental data reported. Also, the calculations showed that HOMO energies could be used as a reactivity descriptor for the selection of collectors, which allows understanding the role of collectors in the initial adsorption step of the flotation processes for acanthite (Ag_2S).

Consequently, these studies demonstrated that molecular modeling using metal ions to represent mineral surface could be used in our work to analyze qualitatively the collector's interaction (PAX and IPETC) with the copper ions (Cu(I) and Cu(II)) contained on the covellite surface. Also, a flotation test could be used to support the findings obtained by DFT calculations. Nevertheless, a disadvantage of using metal ions in molecular modeling is that it does not explore the adsorption mechanism. Several interactions such as chemisorption, physisorption, formation, and precipitation of a metal collector salt, and others may occur between the mineral surface and collectors[19]. Therefore, the phenomena are very complex and involve high computation costs, and the results frequently are not accurate enough. Then, one way to model this system is to overestimate or simplify some of them due to the difficulties in modeling the system—for instance, the complexity of the covellite structure as was done in the present work.

Despite this, the theoretical calculations allow us to understand the role of these collector molecules in the initial adsorption step of the flotation process. Therefore, the results in this study can be extended in future research, which may be focused on the adsorption mechanisms of PAX and IPETC with the two most stable covellite cleavage surfaces in a periodic crystal plane simulation that contains the copper ions Cu(I) and Cu(II) and comparing these results to explore the adsorption mechanism deeply [12].

The NBO net charge of these binding models is shown in Table 7. As regards the $IPETC^-$, the net atomic charge in S4 drops when the complexes $IPETC^-Cu(I)$ and $IPETC^-Cu(II)$ are formed, suggesting an interaction between collectors and both copper ions. The reduction in Cu(I) and Cu(II) net charges demonstrate adsorption as well. The same behavior is identified for PAX^- and the complexes $PAX^-Cu(I)$ and $PAX^-Cu(II)$. The net atomic charges in S3 and S4 decrease after their interaction. In general, it can be seen that collectors interact with both copper ions. Nevertheless, there is a stronger interaction between Cu(II) and collectors, which is evident from its oxidation state. Additionally, these results clarify that copper's interaction with $IPETC^-$ occurs strongly via S4–Cu binding and that with PAX^- occurs via S3–Cu and S4–Cu binding, confirming the XPS results.

Table 7. NBO net atomic charges of $IPETC^-$ and PAX^- and the corresponding complexes

Element	$IPETC^-$	$IPETC^-Cu(I)$	$IPETC^-Cu(II)$	Element	PAX^-	$PAX^-Cu(I)$	$PAX^-Cu(II)$
C1	+0.41	+0.40	+0.41	C2	+0.00	+0.02	+0.05
O2	-0.58	-0.63	-0.64	O1	-0.53	-0.50	-0.46
N3	-0.64	-0.58	-0.49	S3	-0.42	-0.29	-0.09
S4	-0.65	-0.49	-0.21	S4	-0.39	-0.28	-0.11
Cu		+0.74	+1.28	Cu		+0.67	+1.18

More evidence of complex formation between $IPETC^-$ and PAX^- collectors and copper ions was adopted to discuss the bond order variation. The bond order is the number of chemical bonds between a pair of atoms. This method gives the stability and strength of the bond between a pair of atoms. There are many different quantum-chemical definitions of the bond order because it is not a quantum-mechanical observable, and this term is not semantically precise [69–71]. The Wiberg bond index [69] is useful and extensively utilized as a binding analyzer and allows us to calculate the bond strength associated with the main atoms of the molecules and the complexes formed and is provided by the Gaussian package. Table 8 displays the Wiberg bond indices for $IPETC^-$ and PAX^-, and the complexes formed with copper. As regards $IPETC^-$, the Wiberg bond of the C1–S4 became smaller as a result of the electron transfer to copper ions. Additionally, the C1–N3 bond increased, perhaps due to the N atom offering its electron to compensate for the vacant position in the C=S group. The Cu–S4's Wiberg indexes are approximately 0.53 for Cu(I) and 0.64 for Cu(II), indicating new bonds were formed between copper and $IPETC^-$. The Wiberg bond indexes for Cu–O2, Cu–N3, and Cu–C1 are negligible.

As regards PAX^-, the Wiberg bonds for the C2–S3 and C2–S4 became smaller as a result of the electron transfer to copper ions. The Cu–S3's Wiberg bond is approximately 0.44 for Cu(I) and 0.49 for Cu(II). The Cu–S4's Wiberg bond index is around 0.40 for Cu(I) and 0.46 for Cu(II), indicating new bonds formed between copper ions and PAX^-. The Cu–O2 and Cu–C2 Wiberg bonds are negligible. In summary, binding occurs through the C=S group of $IPETC^-$ and through the C=S and C–S groups of PAX^-. This is evident in the binding model shown in Fig. 10a and 10b. The Wiberg bond results agree with the XPS and FT-IR results, demonstrating that DFT calculations are an excellent alternative when studying adsorption mechanisms between minerals and collectors.

Table 8. Wiberg bond indices for $IPETC^-$ and PAX^-, and the complexes formed with copper.

Species	C1–S4	C1–O2	C1–N3	Cu–S4	Cu–O2	Cu–N3	Cu–C1
$(IPETC)^-$	1.1976	0.9696	1.6671	-	-	-	-
$(IPETC)^-(Cu)^+$	1.1158	0.9185	1.7570	0.5291	0.1323	0.0331	0.0611
$(IPETC)^-(Cu)^{++}$	1.0649	0.9427	1.7945	0.6433	0.1205	0.0495	0.0304
Species	**C2–S3**	**C2–S4**	**C2–O1**	**Cu–S3**	**Cu–S4**	**Cu–O2**	**Cu–C2**
$(PAX)^-$	1.4018	1.4462	1.0466	-	-	-	-
$(PAX)^-(Cu)^+$	1.3307	1.3649	1.1202	0.4393	0.4074	0.0486	0.1074
$(PAX)^-(Cu)^{++}$	1.3129	1.3399	1.1959	0.4922	0.4629	0.0309	0.0515

Finally, this work demonstrated that covellite flotation is not pH-dependent in the range employed. Thus, pH could be used for the selective flotation of covellite against pyrite. FT-IR identified the presence of gypsum on the covellite's surface, and XPS shows that gypsum modifies the covellite oxidation state. Nevertheless, it was demonstrated that the gypsum was dissolved, and the collectors were adsorbed on the covellite surface, improving its floatability. Therefore, it is expected that the gypsum does not affect the floatability of the covellite if its quantity is below the solubility level (~2.1 g/L.). As regards the effect of the collector, the covellite floats very well with both collectors, but covellite recovery increases as a result of increasing the collector concentration until it becomes constant. Consequently, there are optimal concentrations that must be determined for specific ores. Nevertheless, higher recoveries were achieved using PAX. Therefore, all these findings could be used in the selective flotation of covellite against pyrite, allowing us to find the optimal conditions for collector type, collector concentration, and pH to be implemented for covellite flotation.

Conclusions

Covellite flotation is not pH-dependent, and its recovery increases significantly with collector concentration. The FT-IR spectra of IPETC indicate that the collector adsorption on the covellite surface is not pH-dependent. The bands related to –C(=S)–NH, –C–H, NH deformation and CH deformation and CNC characteristic of IPETC were present in the spectra demonstrating IPETC adsorption on covellite surface. Nevertheless, the NH stretching band was absent. On the other hand, the FT-IR spectra of PAX show that collector adsorption on the covellite surface is not pH-dependent. PAX adsorption was identified via the leading functional groups, such as dixantogen $(AX)_2$, which formed via vibrational mode C=S, and the Cu-amylxanthate (CuAX).

Additionally, the high-resolution XPS spectra of the Cu 2p spectrum shows that the oxidation state of covellite with PAX is Cu(I). This finding was corroborated by FT-IR by the identification of Cu-amylxanthate (CuAX) and dixantogen $(AX)_2$ on the covellite surface. The adsorption mechanism of IPETC suggests the bind is facilitated by the S of the collector with Cu atoms on the covellite surface. Moreover, the S 2p spectrum of covellite treated with IPETC displays a principal doublet attributed to S_2^{2-} (C=S functional group), as observed for thiourea. Also, the Cu 2p spectrum shows a single sharp peak attributed to the CuS(I) and a minor peak attributed to the CuS(II). The peak related to CuO demonstrated that the covellite was oxidized. Additionally, it was found that the NH was not adsorbed onto covellite surface.

Lastly, the DFT results are in good accordance with the FT-IR and XPS results. The reactive site in the $IPETC^-$ collector was the =S element, and bond with copper only occurred through the C=S group. For PAX^-, the reactive sites were =S and –S elements. Thus, the bond with copper occurred through C=S and C–S groups. The global reactivity descriptor calculations demonstrate that PAX^- has a powerful collector capacity and, therefore, low stability compared to $IPETC^-$. This result agrees with the results obtained from microflotation tests; specifically, the higher recovery with PAX^- (93%) than with $IPETC^-$ (88%). Additionally, it was demonstrated that copper charge matters when it interacts with the collector. In general, the NBO net atomic charges and the Wiberg bond indices show that Cu(II)'s binding with both collectors has stronger energy than Cu(I). This result could be helpful when selecting collectors.

Acknowledgments

This publication was supported by Agencia Nacional de Investigación y Desarrollo de Chile (ANID), Anillo-Grant ACT210027 and Fondecyt 1211498. Y.B acknowledges the infrastructure

and support of the Programa de Doctorado en Ingeniería de Procesos Minerales of Universidad de Antofagasta. Y.B also acknowledges the ANID scholarship Grant 21210801. This work was partially done by Luis Cisternas into visit at the Université du Québec, supported by MINEDUC-UA project, code ANT1999.

Authors and Contributions

Yesica L. Botero. Conceptualization, methodology, experimental test, formal analysis, writing—original draft, review, and editing.

Andres Canales. Molecular modeling methodology and formal analysis.

Rodrigo Serna-Guerrero. Writing—review and editing, supervision, funding acquisition.

Alejandro López-Valdivieso. Conceptualization, supervision, formal analysis.

Mostafa Benzaazoua. Supervision.

Luis Cisternas. Writing—review and editing, conceptualization, methodology, formal analysis, supervision, project administration, funding acquisition.

References

[1] A. Elshkaki, T.E. Graedel, L. Ciacci, B.K. Reck, Copper demand, supply, and associated energy use to 2050, Global Environmental Change. 39 (2016) 305–315. https://doi.org/10.1016/j.gloenvcha.2016.06.006.

[2] L.A. Cisternas, J.I. Ordóñez, R.I. Jeldres, R. Serna-Guerrero, Toward the Implementation of Circular Economy Strategies: An Overview of the Current Situation in Mineral Processing, Mineral Processing and Extractive Metallurgy Review. 00 (2021) 1–23. https://doi.org/10.1080/08827508.2021.1946690.

[3] MINING-DOT-COM, Copper price scales $9,000 after Goldman calls it the new oil, (2021). https://www.mining.com/copper-price-scales-9000-after-goldman-calls-it-the-new-oil/ (accessed April 13, 2021).

[4] D.R. Burrows, M. Rennison, D. Burt, R. Davies, The Onto Cu-Au Discovery, Eastern Sumbawa, Indonesia: A Large, Middle Pleistocene Lithocap-Hosted High-Sulfidation Covellite-Pyrite Porphyry Deposit, Economic Geology. 115 (2020) 1385–1412. https://doi.org/10.5382/econgeo.4766.

[5] E.J. Lam, V. Zetola, Y. Ramírez, Í.L. Montofré, F. Pereira, Making Paving Stones from Copper Mine Tailings as Aggregates, International Journal of Environmental Research and Public Health. 17 (2020) 2448. https://doi.org/10.3390/ijerph17072448.

[6] X. Tian, X. Li, P. Bi, Effect of O-isobutyl-N-ethyl thionocarbamates on flotation behavior of porphyry copper ore and its adsorption mechanism, Applied Surface Science. 503 (2020) 144313. https://doi.org/10.1016/j.apsusc.2019.144313.

[7] N.O. Lotter, D.J. Bradshaw, A.R. Barnes, Classification of the Major Copper Sulphides into semiconductor types, and associated flotation characteristics, Minerals Engineering. 96–97 (2016) 177–184. https://doi.org/10.1016/j.mineng.2016.05.016.

[8] W. Yin, B. Yang, Y. Fu, F. Chu, J. Yao, S. Cao, Z. Zhu, Effect of calcium hypochlorite on flotation separation of covellite and pyrite, Powder Technology. 343 (2019) 578–585. https://doi.org/10.1016/j.powtec.2018.11.048.

[9] J.R. Roos, J.P. Celis, A.S. Sudarsono, Electrochemical control of chalcocite and covellite-xanthate flotation, International Journal of Mineral Processing. 29 (1990) 17–30. https://doi.org/10.1016/0301-7516(90)90003-H.

[10] G.B. Raju, W. Forsling, Adsorption mechanism of diethyldithiocarbamate on covellite, cuprite and tenorite, Colloids and Surfaces. 60 (1991) 53–69. https://doi.org/10.1016/0166-6622(91)80268-S.

[11] M. Porento, P. Hirva, A theoretical study on the interaction of sulfhydryl surfactants with a covellite (001) surface, Surface Science. 555 (2004) 75–82. https://doi.org/10.1016/j.susc.2004.02.033.

[12] A.L. Soares, E.C. dos Santos, Á. Morales-García, H.A. Duarte, H.A. de Abreu, The Stability and Structural, Electronic and Topological Properties of Covellite (001) Surfaces., ChemistrySelect. 1 (2016) 2730–2741. https://doi.org/10.1002/slct.201600422.

[13] N. Karikalan, R. Karthik, S.-M. Chen, C. Karuppiah, A. Elangovan, Sonochemical Synthesis of Sulfur Doped Reduced Graphene Oxide Supported CuS Nanoparticles for the Non-Enzymatic Glucose Sensor Applications, Scientific Reports. 7 (2017) 2494. https://doi.org/10.1038/s41598-017-02479-5.

[14] K.M. Rosso, M.F. Hochella, A UHV STM/STS and ab initio investigation of covellite {001} surfaces, Surface Science. 423 (1999) 364–374. https://doi.org/10.1016/S0039-6028(98)00941-8.

[15] S.S. Kalanur, H. Seo, Synthesis of Cu x S Thin Films with Tunable Localized Surface Plasmon Resonances, ChemistrySelect. 3 (2018) 5920–5926. https://doi.org/10.1002/slct.201800441.

[16] A. Morales-García, A.L. Soares, E.C. dos Santos, H.A. de Abreu, H.A. Duarte, First-Principles Calculations and Electron Density Topological Analysis of Covellite (CuS), The Journal of Physical Chemistry A. 118 (2014) 5823–5831. https://doi.org/10.1021/jp4114706.

[17] G. Fairthorne, D. Fornasiero, J. Ralston, Solution properties of thionocarbamate collectors, International Journal of Mineral Processing. 46 (1996) 137–153. https://doi.org/10.1016/0301-7516(95)00008-9.

[18] P.K. Ackerman, G.H. Harris, R.R. Klimpel, F.F. Aplan, Evaluation of flotation collectors for copper sulfides and pyrite, I. Common sulfhydryl collectors, International Journal of Mineral Processing. 21 (1987) 105–127. https://doi.org/10.1016/0301-7516(87)90009-3.

[19] M. Porento, P. Hirva, Theoretical studies on the interaction of anionic collectors with Cu + , Cu 2+ , Zn 2+ and Pb 2+ ions, Theoretical Chemistry Accounts: Theory, Computation, and Modeling (Theoretica Chimica Acta). 107 (2002) 200–205. https://doi.org/10.1007/s00214-001-0316-8.

[20] A.N. Buckley, G.A. Hope, K.C. Lee, E.A. Petrovic, R. Woods, Adsorption of O-isopropyl-N-ethyl thionocarbamate on Cu sulfide ore minerals, Minerals Engineering. 69 (2014) 120–132. https://doi.org/10.1016/j.mineng.2014.08.002.

[21] G. Zhao, J. Peng, H. Zhong, S. Wang, G.Y. Liu, Synthesis of novel ether thionocarbamates and study on their flotation performance for chalcopyrite, Minerals. 6 (2016). https://doi.org/10.3390/min6030097.

[22] X. Ma, L. Xia, S. Wang, H. Zhong, H. Jia, Structural Modification of Xanthate Collectors To Enhance the Flotation Selectivity of Chalcopyrite, Industrial & Engineering Chemistry Research. 56 (2017) 6307–6316. https://doi.org/10.1021/acs.iecr.6b04566.

[23] J. Mielczarski, E. Suoninen, L.-S. Johansson, K. Laajalehto, An XPS study of adsorption of methyl and amyl xanthates on copper, International Journal of Mineral Processing. 26 (1989) 181–191. https://doi.org/10.1016/0301-7516(89)90028-8.

[24] G. Liu, X. Yang, H. Zhong, Molecular design of flotation collectors: A recent progress, Advances in Colloid and Interface Science. 246 (2017) 181–195. https://doi.org/10.1016/j.cis.2017.05.008.

[25] G. Liu, H. Zhong, T. Dai, L. Xia, Investigation of the effect of N-substituents on performance of thionocarbamates as selective collectors for copper sulfides by ab initio calculations, Minerals Engineering. 21 (2008) 1050–1054. https://doi.org/10.1016/j.mineng.2008.04.017

[26] L. Cisternas, F. Lucay, Y. Botero, Trends in Modeling, Design, and Optimization of Multiphase Systems in Minerals Processing, Minerals. 10 (2019) 22. https://doi.org/10.3390/min10010022.

[27] J.P. Perdew, Y. Wang, Accurate and simple analytic representation of the electron-gas correlation energy, Physical Review B. 45 (1992) 13244–13249. https://doi.org/10.1103/PhysRevB.45.13244.

[28] V.A. Rassolov, J.A. Pople, M.A. Ratner, T.L. Windus, 6-31G * basis set for atoms K through Zn, The Journal of Chemical Physics. 109 (1998) 1223–1229. https://doi.org/10.1063/1.476673.

[29] S.Y. and T.H. Huzinaga S, Andzelm J, Radzio-Andzelm E, Gaussian Basis Sets for Molecular Calculations, Elsevier Science & Techn., 2012.

[30] M.J. Frisch, G.W. Trucks, H.B. Schlegel, G.E. Scuseria, M.A. Robb, J.R. Cheeseman, G. Scalmani, V. Barone, G.A. Petersson, H. Nakatsuji, X. Li, M. Caricato, A. Marenich, J. Bloino, B.G. Janesko, R. Gomperts, B. Mennucci, H.P. Hratchian, J. v. Ortiz, A.F. Izmaylov, J.L. Sonnenberg, D. Williams-Young, F.L. F. Ding, F. Egidi, J. Goings, B. Peng, A. Petrone, T. Henderson, D. Ranasinghe, V.G. Zakrzewski, J. Gao, N. Rega, G. Zheng, W. Liang, M. Hada, M. Ehara, K. Toyota, R. Fukuda, J. Hasegawa, M. Ishida, T. Nakajima, Y. Honda, O. Kitao, H. Nakai, T. Vreven, K. Throssell, J.A. Montgomery, Jr.J.E. Peralta, F. Ogliaro, M. Bearpark, J.J. Heyd, E. Brothers, K.N. Kudin, V.N. Staroverov, T. Keith, R. Kobayashi, J. Normand, K. Raghavachari, A. Rendell, J.C. Burant, S.S. Iyengar, J. Tomasi, M. Cossi, M.K. J. M. Millam, C. Adamo, R. Cammi, J.W. Ochterski, R.L. Martin, K. Morokuma, O. Farkas, J.B. Foresman, D.J. Fox, Gaussian 09, (2016).

[31] R. Dennington, T.A. Keith, J.M. Millam, GaussView, (2016).

[32] J. Tomasi, B. Mennucci, R. Cammi, Quantum Mechanical Continuum Solvation Models, Chemical Reviews. 105 (2005) 2999–3094. https://doi.org/10.1021/cr9904009.

[33] M.D. Hanwell, D.E. Curtis, D.C. Lonie, T. Vandermeersch, E. Zurek, G.R. Hutchison, Avogadro: an advanced semantic chemical editor, visualization, and analysis platform, Journal of Cheminformatics. 4 (2012) 17. https://doi.org/10.1186/1758-2946-4-17.

[34] A.K. Rappe, C.J. Casewit, K.S. Colwell, W.A. Goddard, W.M. Skiff, UFF, a full periodic table force field for molecular mechanics and molecular dynamics simulations, J Am Chem Soc. 114 (1992) 10024–10035. https://doi.org/10.1021/ja00051a040.

[35] D. Cabrera-German, J.A. García-Valenzuela, M. Martínez-Gil, G. Suárez-Campos, Z. Montiel-González, M. Sotelo-Lerma, M. Cota-Leal, Assessing the chemical state of chemically deposited copper sulfide: A quantitative analysis of the X-ray photoelectron spectra of the amorphous-to-covellite transition phases, Applied Surface Science. 481 (2019) 281–295. https://doi.org/10.1016/j.apsusc.2019.03.054.

[36] G.A. Hope, R. Woods, S.E. Boyd, K. Watling, A SERS spectroelectrochemical investigation of the interaction of butylethoxycarbonylthiourea with copper surfaces, Colloids and Surfaces A: Physicochemical and Engineering Aspects. 232 (2004) 129–137. https://doi.org/10.1016/j.colsurfa.2003.10.011.

[37] J.O. Leppinen, C.I. Basilio, R.H. Yoon, FTIR study of thionocarbamate adsorption on sulfide minerals, Colloids and Surfaces. 32 (1988) 113–125. https://doi.org/10.1016/0166-6622(88)80008-8.

[38] Y. Bu, Y. Hu, W. Sun, Z. Gao, R. Liu, Fundamental Flotation Behaviors of Chalcopyrite and Galena Using O-Isopropyl-N-Ethyl Thionocarbamate as a Collector, Minerals. 8 (2018) 115. https://doi.org/10.3390/min8030115.

[39] D.W. Mayo, F.A. Miller, R.W. Hannah, Course Notes on the Interpretation of Infrared and Raman Spectra, John Wiley & Sons, Inc., Hoboken, NJ, USA, 2004. https://doi.org/10.1002/0471690082.

[40] B. Schrader, Infrared and Raman Spectroscopy. methods and applications., VCH Verlagsgesellschsft mbH, Weinheim, Germany, 1995.

[41] J.L. Bishop, M.D. Lane, M.D. Dyar, S.J. King, A.J. Brown, G.A. Swayze, Spectral properties of Ca-sulfates: Gypsum, bassanite, and anhydrite, American Mineralogist. 99 (2014) 2105–2115. https://doi.org/10.2138/am-2014-4756.

[42] H. Marvin, The infrared spectrum of Gypsum CaSO4.2H2O, 1955.

[43] T. Yuan, J. Wang, Z. Li, Measurement and modelling of solubility for calcium sulfate dihydrate and calcium hydroxide in NaOH/KOH solutions, Fluid Phase Equilibria. 297 (2010) 129–137. https://doi.org/10.1016/j.fluid.2010.06.012.

[44] O. Marin, J. Ordoñez, E. Galvez, L. Cisternas, Pourbaix diagrams for copper ores processing with seawater, Physicochemical Problems of Mineral Processing. 56 (2020) 624–640. https://doi.org/10.37190/ppmp/123407.

[45] L.H. Little, G.W. Poling, J. Leja, INFRARED SPECTRA OF XANTHATE COMPOUNDS: II. ASSIGNMENT OF VIBRATIONAL FREQUENCIES, Canadian Journal of Chemistry. 39 (1961) 745–754. https://doi.org/10.1139/v61-090.

[46] M.L. Shankaranarayana, C.C. Patel, INFRARED SPECTRA AND THE STRUCTURES OF XANTHATES AND DIXANTHOGENS, Canadian Journal of Chemistry. 39 (1961) 1633–1637. https://doi.org/10.1139/v61-209.

[47] A.P. Chandra, A.R. Gerson, A review of the fundamental studies of the copper activation mechanisms for selective flotation of the sulfide minerals, sphalerite and pyrite, Advances in Colloid and Interface Science. 145 (2009) 97–110. https://doi.org/10.1016/j.cis.2008.09.001.

[48] H. Peng, D. Wu, M. Abdalla, W. Luo, W. Jiao, X. Bie, Study of the Effect of Sodium Sulfide as a Selective Depressor in the Separation of Chalcopyrite and Molybdenite, Minerals. 7 (2017) 51. https://doi.org/10.3390/min7040051.

[49] J.C.W. Folmer, F. Jellinek, The valence of copper in sulphides and selenides: An X-ray photoelectron spectroscopy study, Journal of The Less-Common Metals. 76 (1980) 153–162. https://doi.org/10.1016/0022-5088(80)90019-3.

[50] J.T. Kloprogge, B.J. Wood, Handbook of Mineral Spectroscopy, Elsevier, 2020. https://doi.org/10.1016/C2015-0-01704-X.

[51] S.W. Goh, A.N. Buckley, R.N. Lamb, Copper(II) sulfide?, Minerals Engineering. 19 (2006) 204–208. https://doi.org/10.1016/j.mineng.2005.09.003.

[52] Thermo scientific XPS simplified, (n.d.). https://xpssimplified.com/.

[53] NIST X-ray Photoelectron Spectroscopy Database, NIST Standard Reference Database Number 20, (2000). https://doi.org/:10.18434/T4T88K.

[54] X-ray Photoelectron Spectroscopy (XPS) Reference Pages, (n.d.). http://www.xpsfitting.com/.

[55] I. Nakai, Y. Sugitani, K. Nagashima, Y. Niwa, X-ray photoelectron spectroscopic study of copper minerals, Journal of Inorganic and Nuclear Chemistry. 40 (1978) 789–791. https://doi.org/10.1016/0022-1902(78)80152-3.

[56] M. Kundu, T. Hasegawa, K. Terabe, K. Yamamoto, M. Aono, Structural studies of copper sulfide films: Effect of ambient atmosphere, Science and Technology of Advanced Materials. 9 (2008). https://doi.org/10.1088/1468-6996/9/3/035011.

[57] S.W. Goh, A.N. Buckley, R.N. Lamb, R.A. Rosenberg, D. Moran, The oxidation states of copper and iron in mineral sulfides, and the oxides formed on initial exposure of chalcopyrite and bornite to air, Geochimica et Cosmochimica Acta. 70 (2006) 2210–2228. https://doi.org/10.1016/j.gca.2006.02.007.

[58] M.C. Biesinger, L.W.M. Lau, A.R. Gerson, R.S.C. Smart, Resolving surface chemical states in XPS analysis of first row transition metals, oxides and hydroxides: Sc, Ti, V, Cu and Zn, Applied Surface Science. 257 (2010) 887–898. https://doi.org/10.1016/j.apsusc.2010.07.086.

[59] D.M. Ávila-Márquez, I.A. Reyes-Domínguez, A. Blanco-Flores, H.P. Toledo-Jaldin, G. López-Téllez, J. Aguilar-Carrillo, E.J. Gutiérrez-Castañeda, Study of the Influence of Xanthate Derivative Structures on Copper Sulfide Mineral Adsorption Under Acidic Conditions, Metallurgical and Materials Transactions B. 50 (2019) 86–97. https://doi.org/10.1007/s11663-018-1452-z.

[60] M. Miar, A. Shiroudi, K. Pourshamsian, A.R. Oliaey, F. Hatamjafari, Theoretical investigations on the HOMO–LUMO gap and global reactivity descriptor studies, natural bond orbital, and nucleus-independent chemical shifts analyses of 3-phenylbenzo[d]thiazole-2(3 H)-imine and its para -substituted derivatives: Solvent and, Journal of Chemical Research. 45 (2021) 147–158. https://doi.org/10.1177/1747519820932091.

[61] K. Fukui, Role of Frontier Orbitals in Chemical Reactions, Science (1979). 218 (1982) 747–754. https://doi.org/10.1126/science.218.4574.747.

[62] The prediction and theoretical study for chemical reactivity, thermophysical and biological activity of morpholinium nitrate and nitrite ionic liquid crystals: A DFT

study, Advanced Journal of Chemistry-Section A. 2 (2019) 316–326. https://doi.org/10.33945/SAMI/AJCA.2019.4.5.

[63] V. Choudhary, A. Bhatt, D. Dash, N. Sharma, DFT calculations on molecular structures, HOMO–LUMO study, reactivity descriptors and spectral analyses of newly synthesized diorganotin(IV) 2-chloridophenylacetohydroxamate complexes, Journal of Computational Chemistry. 40 (2019) 2354–2363. https://doi.org/10.1002/jcc.26012.

[64] C.-G. Zhan, J.A. Nichols, D.A. Dixon, Ionization Potential, Electron Affinity, Electronegativity, Hardness, and Electron Excitation Energy: Molecular Properties from Density Functional Theory Orbital Energies, The Journal of Physical Chemistry A. 107 (2003) 4184–4195. https://doi.org/10.1021/jp0225774.

[65] V.A. Ignatkina, Selection of selective collectors for flotation of minerals with similar flotation properties, Russian Journal of Non-Ferrous Metals. 52 (2011) 1–7. https://doi.org/10.3103/S1067821211010093.

[66] G. Zhao, J. Peng, H. Zhong, S. Wang, G. Liu, Synthesis of Novel Ether Thionocarbamates and Study on Their Flotation Performance for Chalcopyrite, Minerals. 6 (2016) 97. https://doi.org/10.3390/min6030097.

[67] B. Bag, B. Das, B.K. Mishra, Geometrical optimization of xanthate collectors with copper ions and their response to flotation, Minerals Engineering. 24 (2011) 760–765. https://doi.org/10.1016/j.mineng.2011.01.006.

[68] G. Zhao, H. Zhong, X. Qiu, S. Wang, Y. Gao, Z. Dai, J. Huang, G. Liu, The DFT study of cyclohexyl hydroxamic acid as a collector in scheelite flotation, Minerals Engineering. 49 (2013) 54–60. https://doi.org/10.1016/j.mineng.2013.04.025.

[69] K.B. Wiberg, Application of the pople-santry-segal CNDO method to the cyclopropylcarbinyl and cyclobutyl cation and to bicyclobutane, Tetrahedron. 24 (1968) 1083–1096. https://doi.org/10.1016/0040-4020(68)88057-3.

[70] D.W. Szczepanik, J. Mrozek, Ground-state projected covalency index of the chemical bond, Computational and Theoretical Chemistry. 1023 (2013) 83–87. https://doi.org/10.1016/j.comptc.2013.09.008.

[71] O. v. Sizova, A.Yu. Sokolov, L. v. Skripnikov, V.I. Baranovski, Quantum chemical study of the bond orders in the ruthenium, diruthenium and dirhodium nitrosyl complexes, Polyhedron. 26 (2007) 4680–4690. https://doi.org/10.1016/j.poly.2007.04.008.

APPENDIX A

This appendix contains a diagram of the modified Hallimond-type flotation cell (Fig. A1). The XPS survey scan of covellite and washed covellite is shown in Fig. A2. The survey was indexed with the main peaks of covellite. Moreover, we identified the Ca^{2+} element, located at 348 eV and 351 eV, as

attributed to Ca $2p_{3/2}$ and Ca $2p_{1/2}$, respectively. Then, the peak located at 169-170 eV and labeled S $2p_{3/2}$ and S $2p_{1/2}$ was attributed to the elemental species ion SO_4^{2-} [48]. The Ca^{2+} and SO_4^{2-} disappeared once the covellite was washed, confirming the solubilization of gypsum. Additionally, the XPS high-resolution spectra of Cu 2p, C 1s, S 2p, and O 1s, recorded from the covellite treated with PAX and covellite treated with IPETC at Ph 8 and 11, are shown in Fig. A3-A6. These XPS spectra demonstrate that changes in Ph (from 8 to 11) do not affect the adsorption of PAX and IPETC on the covellite surface. Finally, Table A1 presents the atomic concentrations of elements for covellite, and covellite treated with PAX and IPETC at Ph 8 and 11, determined by XPS.

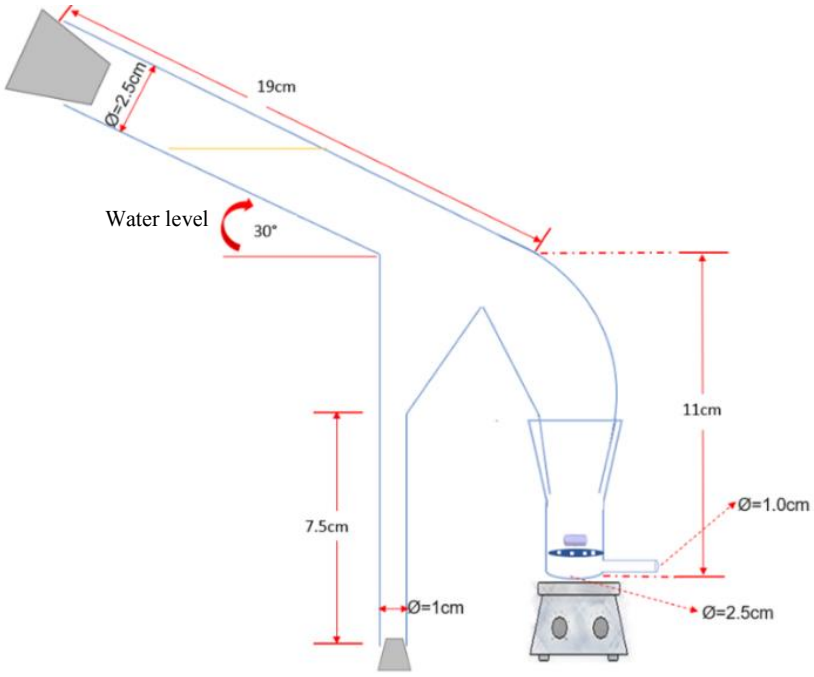

Fig. A1. Diagram of modified Hallimond-type flotation cell.

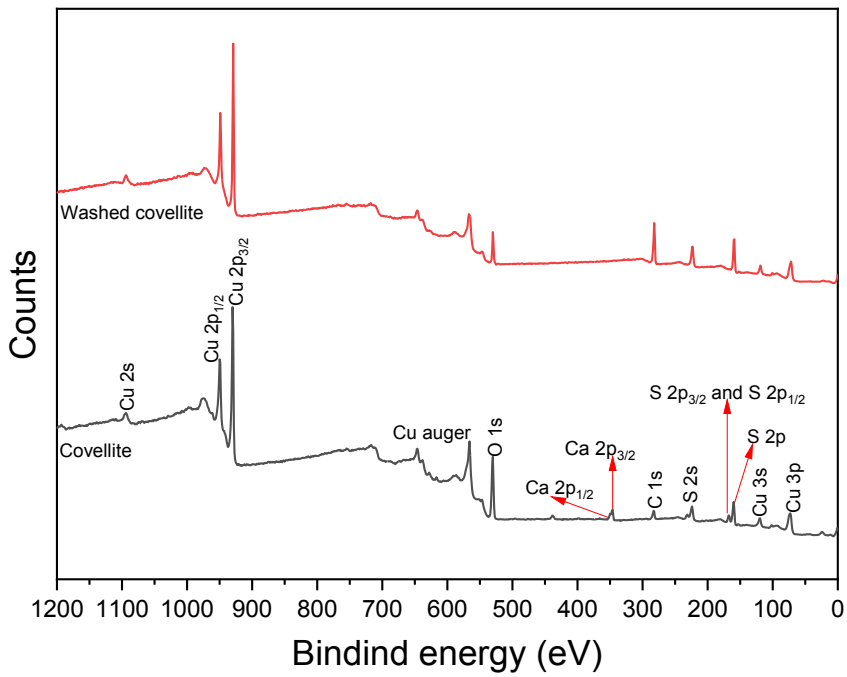

Fig. A2. XPS survey spectrum for covellite and washed covellite.

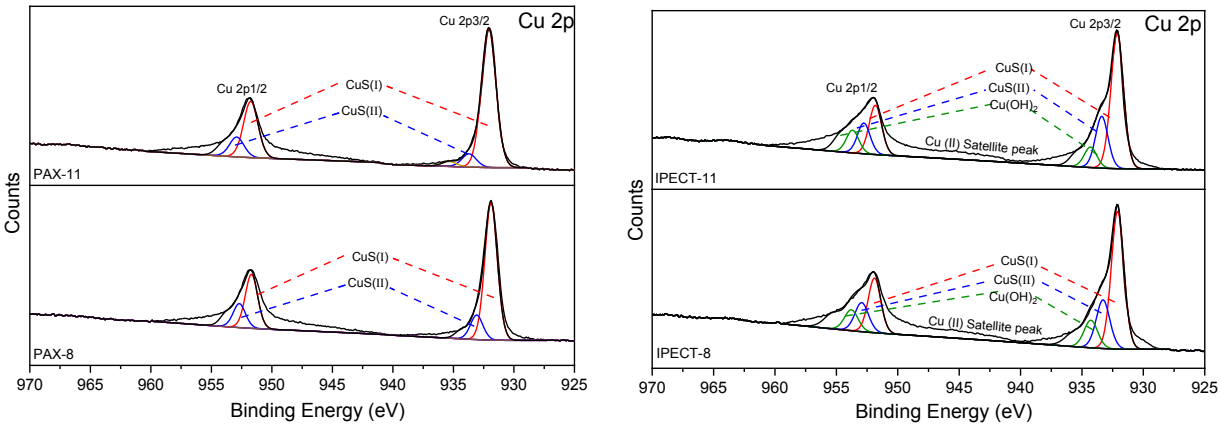

Fig. A3. XPS Cu 2p spectrum for covellite with PAX and IPETC at pH 8 and 11.

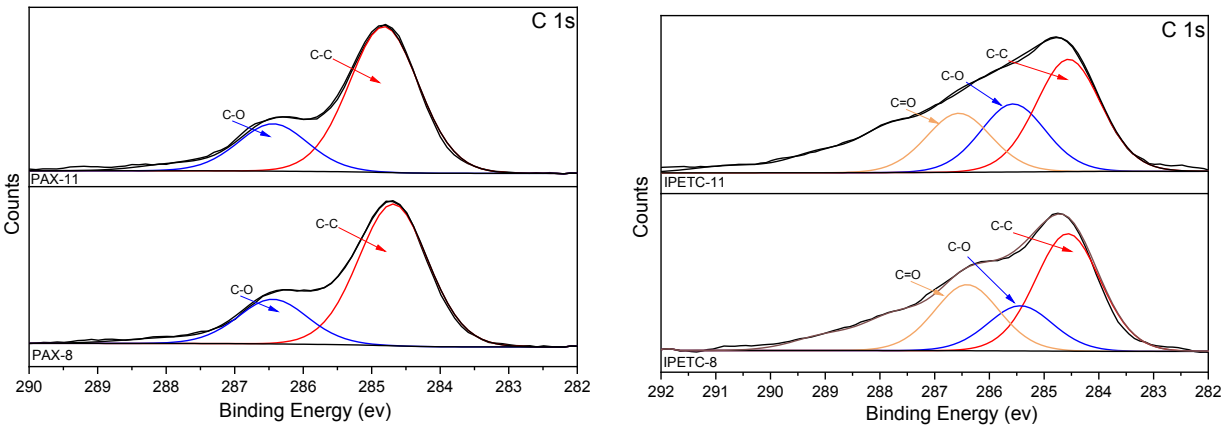

Fig. A4. XPS C 1s spectrum for covellite with PAX and IPETC at pH 8 and 11.

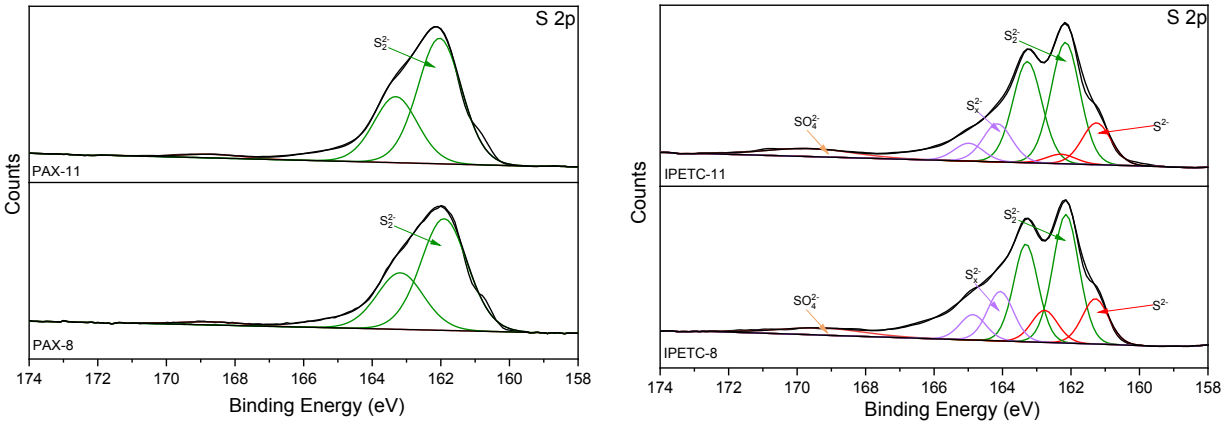

Fig. A5. XPS S 2p spectrum for covellite with PAX and IPETC at pH 8 and 11.

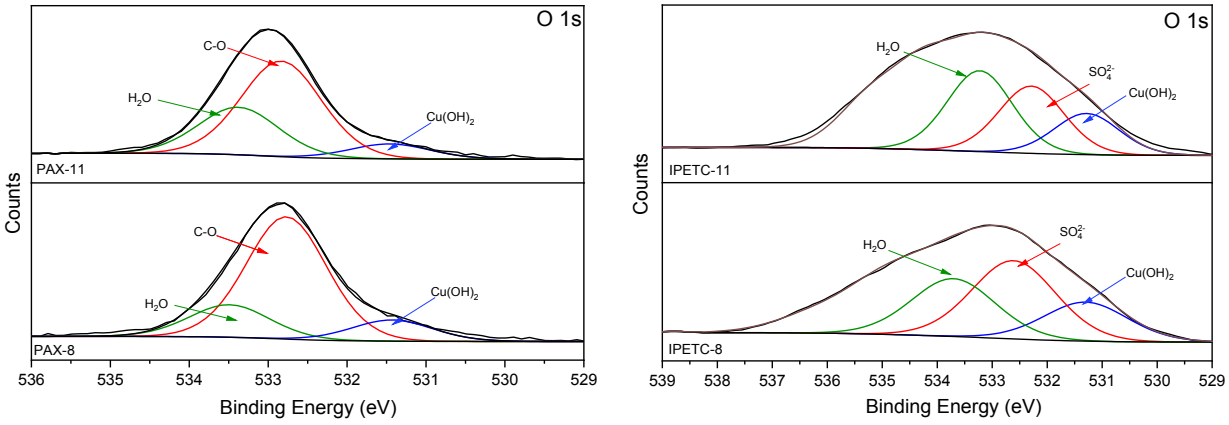

Fig. A6. XPS O 1s spectrum for covellite with PAX and IPETC at pH 8 and 11.

Table A1. Atomic concentrations of elements in covellite, and covellite treated with PAX and IPETC at pH 8 and 11, determined by XPS.

	Atomic concentration (%)						**Atomic concentration ratio to Cu (%)**					
	Cu 2p	**O 1s**	**N 1s**	**C 1s**	**S 2p**	**Ca 2p**	**Cu 2p**	**O 1s**	**N 1s**	**C 1s**	**S 2p**	**Ca 2p**
CuS	21.98	35.11	1.64	15.52	22	3.75	1	1.60	0.07	0.71	1.00	0.17
PAX-8	18.85	12.06	0.18	46.84	21.73	0.35	1	0.64	0.01	2.48	1.15	0.02
Δ	-3.13	-23.05	-1.46	31.32	-0.27	-3.4	0	-0.96	-0.07	1.78	0.15	-0.15
PAX-11	18.08	12.07	0	48.6	21.12	0.13	1	0.67	0.00	2.69	1.17	0.01
Δ	-3.9	-23.04	-1.64	33.08	-0.88	-3.62	0	-0.93	-0.07	1.98	0.17	-0.16
IPETC-8	33.97	15.65	0.97	20.85	28.56	0	1	0.46	0.03	0.61	0.84	0.00
Δ	11.99	-19.46	-0.67	5.33	6.56	-3.75	0	-1.14	-0.05	-0.09	-0.16	-0.17
IPETC-11	34.41	10.21	0	26.95	28.23	0.19	1	0.30	0.00	0.78	0.82	0.01
Δ	12.43	-24.9	-1.64	11.43	6.23	-3.56	0	-1.30	-0.07	0.08	-0.18	-0.17

Δ is defined as the value after PAX and IPETC treatment minus that before treatment.